Impact of Radiatively Interactive Dust Aerosols in the NASA GEOS-5 Climate Model: Sensitivity to Dust Particle Shape and Refractive Index

Peter R. Colarco[1], Edward P. Nowottnick[1,2], Cynthia A. Randles[1,3], Bingqi Yi[4], Ping Yang[4], Kyu-Myong Kim[1,3], Jamison A. Smith[5], Charles G. Bardeen[6]

[1]Laboratory for Atmospheric Chemistry and Dynamics, NASA GSFC

[2]NASA Postdoctoral Program

[3]GESTAR/Morgan State University

[4]Department of Atmospheric Sciences, Texas A&M University

[5]Laboratory for Atmospheric and Space Physics, University of Colorado

[6]National Center for Atmospheric Research

Abstract

We investigate the radiative effects of dust aerosols in the NASA GEOS-5 atmospheric general circulation model. A sectional aerosol and cloud microphysics model (CARMA) is included in GEOS-5. CARMA treats the dust aerosol lifecycle, including sources, transport evolution, and sinks. The CARMA aerosols are radiatively coupled to GEOS-5, and we perform a series of AMIP-style simulations in which dust optical properties (spectral refractive index and particle shape) are varied. Spherical dust optical properties are from Mie theory, while non-spherical properties are drawn from a recent database for tri-axial ellipsoids. The simulated dust distributions generally compare well to data from the space-based MODIS, MISR, and CALIOP, the ground-based AERONET, and surface measurements of dust deposition and mass concentration. We show significant variability in simulated summertime Saharan dust distributions resulting from different choices of dust optical

properties. Dust atmospheric heating enhances surface winds over important dust sources, increasing emissions. We find that increased dust absorption leads to a strengthening of the summertime Hadley cell circulation, increasing dust lofting to higher altitudes, and strengthening the African Easterly Jet. This leads to a longer atmospheric residence time and generally more northward transport of dust in simulations with the most absorbing dust optical properties, in best agreement with observations. We find that particle shape has a minor effect on dust transport and distribution, although total atmospheric forcing is enhanced by as much as 30% over land for simulations incorporating a spheroidal shape distribution versus ellipsoidal or spherical shapes.

1. Introduction

Mineral dust aerosols play many roles in Earth's climate system. Scattering and absorption of shortwave (i.e., solar) and longwave (i.e., thermal) radiation by dust particles directly influence Earth's radiation balance (Sokolik and Toon, 1996; Balkanski et al., 2007). The indirect effect of dust particles on climate includes their modification of cloud properties. For example, by acting as an additional source of cloud condensation nuclei (CCN), dust particles can lead to smaller cloud droplets, hence limiting droplet coalescence efficiency and suppressing precipitation (Rosenfeld et al., 2001). The facility of dust particles to act as ice nuclei in clouds offers another pathway toward indirect climate effects, where dust is observationally linked to glaciation in mildly super-cooled altocumulus clouds (Sassen et al., 2003). Dry air layers associated with Saharan dust outbreaks may play a role in suppressing convection and tropical cyclone formation in the Atlantic (Dunion and Velden, 2004; Wong and Dessler, 2005), and satellite observations suggest an inverse relationship

between the presence of dust and tropical cyclone activity in the same region (Evan et al., 2006; Lau and Kim, 2007). Observational evidence from meteorological analyses suggests a role for radiative heating of Saharan dust layers in modulating the amplitude of easterly waves in which the dust is typically transported (Jones et al., 2004). Biological productivity (i.e., photosynthetic activity in phytoplankton) in many ocean regions is limited by the availability of iron, which has as a major and variable source the deposition of mineral dust aerosols (Martin, 1990; Fung et al., 2000; Mahowald et al., 2009). To the extent that an enhanced supply of nutrients from dust deposition mitigates the iron stress limitation in these ecosystems, dust can modulate the oceanic uptake of CO_2 at the ocean-air interface (see review in Jickells et al., 2005). Similarly, dust can be an important nutrient source to terrestrial ecosystems (Swap et al., 1992). Atmospheric dust aerosols play a role in tropospheric photochemistry pathways by altering photolysis rates and acting as a surface on which heterogeneous reactions can occur (Dentener et al., 1996; Bian and Zender, 2003; Bauer et al., 2004). Finally, long-range transport of dust aerosols are a source of fine particulate matter associated with poor air quality episodes (Prospero, 1999) and are a vector for transporting microorganisms associated with coral reef mortality (Shinn et al., 2000).

Because of the importance of mineral dust aerosols in Earth's climate system there has been a considerable effort to model their temporally and spatially varying distributions in chemical transport models and global climate models (Tegen and Fung, 1994; Mahowald et al., 1999; Ginoux et al., 2001; Zender et al., 2003; Colarco et al., 2003; Su and Toon, 2009; Nowottnick et al., 2010). Synthesis studies of various modeling efforts reveal the importance of dust to the total aerosol loading, but also show wide variability in modeled

emissions and atmospheric burden (Zender et al., 2004; Textor et al., 2006; Huneeus et al., 2011). There also remain large differences in the treatment of the particle size distribution and its evolution in dust models that can greatly affect the dust radiative impacts (Kok 2011). These issues are convolved with model-dependent factors that impact source, sink, and transport terms in the aerosol evolution (e.g., spatial resolution, dynamical core, turbulent and convective parameterizations, precipitation, etc.).

The direct radiative effects of dust aerosols on Earth's climate thus remain uncertain in both magnitude and even sign in recent assessments (IPCC 2007). In addition to the uncertainties in atmospheric burden and particle size distribution noted above, there remains an uncertainty in the dust optical properties themselves. These are manifest in the composition of the dust—generally a function of source and particle size—and these will have important effects on the radiative properties of the aerosol (Sokolik and Toon, 1999; Quijano et al., 2000). The typical modeling paradigm is to carry the size resolved mass of dust as a number of tracers, and for each tracer to specify optical properties that are a function of size and the spectrally varying complex index of refraction. Often the refractive indices are derived from measurements based on *in situ* dust samples (e.g., Shettle and Fenn, 1979; Hess et al., 1998). Optical properties derived from these measurements suggest considerably more shortwave absorption by dust than do properties inferred from space-based remote sensing techniques (Kaufman et al., 2001; Moulin et al., 2001; Colarco et al., 2002; Sinyuk et al., 2003). Retrievals from sun photometer observations also suggest very weakly absorbing dust in the shortwave (Kim et al., 2011). Overall, dust absorption as represented by the imaginary component of the refractive index may vary by an order of

93 magnitude among these various datasets (Balkanski et al., 2007). Additionally, spectral
94 dust optical properties are often derived assuming particle sphericity using Mie theory,
95 although it is well known that dust particles are non-spherical. Shape effects are
96 understood to be important to retrieval of aerosol properties from spectral, angular, and
97 polarized reflectance measurements (e.g., Feng et al., 2009), but the importance to flux
98 calculations like those performed in GCM radiative transfer schemes has been thought to be
99 small (Mishchenko et al., 1995). Recently, however, improved databases of optical
100 properties for non-spherical dust-like aerosols suggest uncertainties in top of atmosphere
101 (TOA) fluxes of as much as 30% due to dust shape effects (Yi et al., 2011). While that figure
102 is likely on the high end for the effects of non-spherical particles, we are not aware of global
103 aerosol modeling studies that have incorporated the effects of dust shape in their radiative
104 forcing studies. This provides a motivation for the present study.
105
106 In this study we investigate the impact of dust optical properties on the simulation of the
107 dust aerosol lifecycle in the NASA Goddard Earth Observing System (GEOS) atmospheric
108 general circulation model. An aerosol and cloud microphysics model has been
109 incorporated into the GEOS environment, and parameterizations for dust and sea salt
110 aerosol sources and sinks have been included. The tracers in the aerosol module are
111 transported online in the GEOS AGCM and are radiatively coupled through the radiative
112 transfer scheme, allowing for the inclusion of the aerosol direct radiative effect and the
113 associated semi-direct effect on clouds in the model climate. The aerosol indirect effect is
114 not considered in this study. A number of simulations are conducted in which we vary the
115 dust optical properties both in terms of the particle shape and the spectrally varying index

of refraction. In Section 2 we describe the model and the dust optical properties used. In Section 3 we evaluate our simulations with observational datasets. In Section 4 we discuss the impact of the dust optical properties on the climate of the model. We present conclusions in Section 5.

2. Model Description

2.1. NASA Goddard Earth Observing System model, version 5 (GEOS-5)

The GEOS-5 atmospheric general circulation model (AGCM) is one of the main components of the GEOS-5 atmospheric data assimilation system and earth system model (Rienecker et al., 2008). GEOS-5 is used to provide (i) research quality atmospheric reanalyses for use by the scientific community (e.g. the Modern-Era Retrospective Analysis for Research and Applications or MERRA, Rienecker et al., 2011), (ii) forward-processed analyses and forecasts for use by NASA instrument teams (e.g. Zhu and Gelaro, 2008), and (iii) analyses and forecasts for use in various field campaigns (e.g. Bian et al., 2013). It has also been used as a tool to study aerosol impacts on weather (e.g. Reale et al., 2011) and climate (e.g. Ott et al., 2010; Randles et al., 2013) by inclusion of an online aerosol module (Colarco et al., 2010).

The GEOS-5 AGCM simulates traditional meteorological parameters (wind, temperature, pressure, etc.), combining the finite volume dynamical core of Lin (2004) with a column physics package. Turbulence is based on Lock et al. (2000). Convection is from the relaxed Arakawa-Schubert (RAS) scheme (Moorthi and Suarez, 1992) and incorporates a prognostic cloud scheme. Interactions with the land surface are through the catchment model of Koster et al. (2000). Radiative transfer is computed using the parameterization of

Chou and Suarez (1994; 1999) and Chou et al. (2001), incorporating gaseous absorption and scattering and absorption by aerosols in eight shortwave and ten longwave bands. The model can be run at various horizontal spatial resolutions. There are 72 vertical layers distributed in a hybrid sigma coordinate system that is terrain following near the surface and transforming to pressure coordinates near 180 hPa with the model top at 1 Pa (~85km). An integrated ocean circulation model was not yet available when this study was performed, so sea surface temperatures were prescribed (see below).

2.2. Community Aerosol and Radiation Model for Atmospheres (CARMA)

We have coupled the Community Aerosol and Radiation Model for Atmospheres (CARMA, Toon et al., 1988; Jensen et al., 1994; Ackerman et al., 1995) to GEOS-5. CARMA is a sectional aerosol and cloud microphysics model that has been applied to simulate dust (Colarco et al., 2002; 2003; Su et al., 2009), sea salt (Madry et al., 2011; Fan et al., 2011), sulfate (English et al., 2011; 2012), and carbonaceous aerosols (Colarco et al., 2004; Matichuk et al., 2007; 2008). Although the mechanisms in CARMA permit treatment of aerosol growth and nucleation, our setup of CARMA in this study is simple. For dust, we partition the aerosol mass across eight logarithmically spaced size bins spanning radius from 0.1 – 10 μm. This setup is the same as in Colarco et al. (2003). The dust tracers are radiatively coupled to the host model through the GEOS-5 native radiative transfer interface. The only CARMA-based microphysical process affecting the dust tracers is sedimentation; other processes relating to emissions and deposition are described below. Sea salt aerosols are incorporated in a similar fashion (Section 2.5). There is no interaction of the dust and sea salt.

2.3. Dust Emission and Removal Processes

Dust emission and removal processes essentially follow from Colarco et al. (2003) and Colarco et al. (2010). Dust emissions are based on Ginoux et al. (2001), who provide a map of potential dust source locations based on the observed correlation of dust emitting regions with large-scale topographic depressions. In this study the topographic map is updated and provided at a 1° x 1° latitude-by-longitude spatial resolution (P. Ginoux, personal communication) and is remapped in a conservative fashion to the 2° x 2.5° horizontal resolution used in our simulations. Dust emissions are computed at each model time step and grid box as

$$E_{i,j} = s_r \cdot C \cdot S_{i,j} \cdot u_{i,j}^2 \left(u_{i,j} - u_t\right);\ u_{i,j} > u_t \qquad (1)$$

where $S_{i,j}$ is the grid box i,j potential efficiency to act as a dust source (dimensionless with a value 0 – 1 in magnitude) and $u_{i,j}$ is the model wind speed at 10-meter altitude. u_t is the particle size-dependent threshold wind speed that must be exceeded in order to emit dust (Marticorena and Bergametti, 1995). This threshold wind speed is increased for wet soils following Ginoux et al. (2001). s_r is the relative fraction of dust particles existing in the soil at each of our size bins, similar to Colarco et al. (2003). We assume a globally constant distribution for silt-sized particles (1 micron < radius < 10 micron), so s_r = 0.25 for each of the four size bins in that range. We assume that the mass of clay-sized particles (radius < 1 micron) is 10% of the silt mass, and the relative partitioning of the four sub-micron size bins follows from Tegen and Lacis (1996, their Table 1). C is a global tuning constant used to set the overall emissions. In practical terms, since there are no global observations of dust emissions, C is tuned to give a reasonable dust loading or dust aerosol optical

thickness, and is thus model dependent. In all the experiments described in this study we set $C = 0.35\ \mu g\ s^{-2}\ m^{-5}$.

Once emitted, dust is transported by advection, as well as turbulent and convective mixing. Dust is removed by sedimentation (calculated in the CARMA module), or else by turbulent dry deposition and large-scale and convective-scale wet removal, using algorithms that were developed for other aerosol packages implemented in GEOS-5 (see Colarco et al., 2010).

2.4. Dust Optical Properties

The focus of this study is on the impact of the dust direct radiative effect on the GEOS-5 atmospheric model. We therefore consider several variations of the dust optical properties in our simulations in order to investigate this sensitivity. We approach this by varying the assumptions of dust refractive index and particle shape in generating the lookup tables of dust optical properties used by the model. Shape is considered for optical purposes only; we do not investigate the impact of shape on, for example, sedimentation velocities (e.g., Colarco et al., 2003; Ginoux, 2003). We do not explicitly consider mineralogy or how it might vary with source regions, particle size, or during transport. Rather, we prescribe a size-independent refractive index that varies only with wavelength. The dust optical properties will affect the simulation as far as the radiative feedback on the model, and hence the dust lifecycle, but in all other respects the treatment of dust is as described in Section 2.3 and is the same for each sensitivity study.

208 The dust refractive indices are drawn from three sources: (1) the commonly used Optical
209 Properties for Aerosols and Clouds database (OPAC, Hess et al., 1998), (2) the Shettle and
210 Fenn (1979, hereafter referred to as SF) database, and (3) a merger of remote sensing
211 based estimates of dust refractive indices in the shortwave with the SF values in the
212 longwave (referred to hereafter as OBS). The OBS based refractive indices are from
213 Colarco et al. (2002) in the UV (based on simulating the aerosol index from the Total Ozone
214 Mapping Spectrometer) and from Kim et al. (2011) in the visible (based on inversions of
215 the Aerosol Robotic Network sun photometer observations). A log-power law curve is fit to
216 the Colarco et al. (2002) and Kim et al. (2011) refractive indices, joining these smoothly
217 with the SF refractive indices at infrared wavelengths. The real and imaginary components
218 of the refractive index for each of these data sets are shown in Figure 1.
219
220 The optical properties of spherical dust particles are computed using the Mie theory code
221 of Wiscombe (1980). For each of our eight size bins we compute and then integrate the
222 optical properties across 10 sub-size bins assuming dM / d(log r) = constant across the size
223 bin. The optical properties of non-spherical dust particles are derived from the database of
224 Meng et al. (2010), which is a compilation of optical properties for tri-axial ellipsoids based
225 on a combination of the solutions derived from Mie theory, the T-Matrix method
226 (Mishchenko and Travis, 1998), the discrete dipole approximation (DDA) technique
227 (Yurkin and Hoekstra, 2007), and an improved geometric optics method (Yang and Liou,
228 1996). The electromagnetic edge effects (Nussenzveig 1992) are included in the extinction
229 and absorption cross sections for large size parameters in the geometric optics domain.

230 The nodes in the database are refractive index, size parameter, and two values of particle
231 aspect ratio.
232
233 Two shape distributions are considered: a distribution composed primarily of tri-axial
234 ellipsoids based on Yi et al. (2011) and a spheroidal distribution from Dubovik et al.
235 (2006). Spheroids are a special case of tri-axial ellipsoids and are handled in the Meng et
236 al. (2010) database. For a visualization of these shapes see Figure 1 in Meng et al. (2010).
237 For each of our size bins we integrate across a sub-size bin distribution similar to what was
238 done in the Mie theory calculations, with a second integration across the shape
239 distribution.
240
241 Optical properties computed include the mass scattering and extinction efficiencies,
242 asymmetry parameter, and the Legendre polynomial moments of the polarized phase
243 function. Properties are computed at 61 wavelengths spanning 0.25 – 40 microns (the
244 wavelengths considered in the OPAC database). Properties are integrated to the eight
245 shortwave and ten longwave bands used in the GEOS-5 radiation codes using a simple
246 linear averaging. Ultimately we provide GEOS-5 a lookup table of the relevant optical
247 properties (mass extinction efficiency, single scattering albedo, and asymmetry parameter)
248 for each size bin and wavelength band. Table 1 summarizes the optical properties used in
249 each of our simulations. Figure 2 presents the dust optical properties for each of our
250 experiments. Also shown is the deviation of aerosol optical thickness (AOT), single
251 scattering albedo (SSA), and asymmetry parameter (g) from a baseline of the OPAC-
252 Spheres model assuming the summertime climatological dust aerosol particle size

distribution from our OPAC-Spheres model run at Cape Verde (Figure 8, under the main Saharan dust plume). The model evolved aerosol particle size distribution has an effective radius of 2.24 μm, and the total mass loading has been adjusted to give an AOT of 1 at 550 nm wavelength for the OPAC-Spheres set of optical properties. Calculations for other dust optical tables use the same mass loading and particle size distribution, and so Figure 2 emphasizes changes in the dust AOT, SSA, and asymmetry parameter due to changes in the optical tables. Figure 2 shows results for all 61 wavelengths present in our lookup tables. The dust optical properties shown in Figure 2 are summarized for a wavelength of 550 nm in Table 1.

Table 1. Summary of experiments and characteristics.

Experiment Name	Refractive Index	Shape	AOT_{550}	SSA_{550}	g_{550}
No Forcing[a]	OPAC[b]	Spheres	1.00	0.86	0.75
OPAC-Spheres	OPAC	Spheres	1.00	0.86	0.75
OPAC-Spheroids	OPAC	Spheroids[e]	1.26	0.88	0.77
OPAC-Ellipsoids	OPAC	Ellipsoids[f]	1.27	0.88	0.77
SF-Spheres	Shettle and Fenn[c]	Spheres	1.00	0.82	0.76
SF-Ellipsoids	Shettle and Fenn	Ellipsoids	1.24	0.84	0.78
OBS-Spheres	Colarco/Kim & Shettle and Fenn[d]	Spheres	0.98	0.93	0.74
OBS-Spheroids	Colarco/Kim & Shettle and Fenn	Spheroids	1.22	0.92	0.75

[a]In the "No Forcing" run the aerosols are passive tracers. Here the optical properties refer to those which are used to compute the diagnostic aerosol optical thickness.
[b]OPAC refers to dust refractive indices from Hess et al. (1998).
[c]Shettle and Fenn refers to dust refractive indices from Shettle and Fenn (1979).
[d]Colarco/Kim & Shettle and Fenn refers to dust refractive indices merged from Colarco et al. (2002) and Kim et al. (2011) in the UV/Visible and fit by a log-power law curve to merge with the Shettle and Fenn (1979) values in the infrared.
[e]The spheroidal shape distribution is from Dubovik et al. (2006).
[f]The ellipsoidal shape distribution is from Yi et al. (2011).

2.5. Sea salt

Sea salt aerosol was also simulated simultaneously, but externally mixed with the dust. Eight size bins were used here as well, ranging from 0.03 – 10 microns dry radius. The

277 treatment of sea salt is similar to that described in Colarco et al. (2010). The source
278 formulation of Gong (2003) was used to determine emissions and the particle size
279 distribution. Emissions occur only over open ocean and are a function of the 10-m wind
280 speed. Sea salt aerosol is hydrated according to the parameterization of Gerber (1985) as a
281 function of size and relative humidity. The hydration of the aerosol affects its fall velocity
282 and optical properties. The sea salt aerosols are radiatively coupled to GEOS-5, with
283 optical lookup tables generated assuming Mie theory and similar for dust. Refractive
284 indices for the dry salt particles are from the OPAC database. The hydrated optical
285 properties are computed as a function of relative humidity, with water refractive indices
286 from the HITRAN database (Rothman et al., 2009) and assuming a volume average
287 refractive index of the salt and water droplet. The sea salt results are nearly identical in all
288 of our dust sensitivity simulations, and so we do not discuss them further.
289
290 **2.6. Experimental Design**
291 We have nine potential sensitivity experiments to consider: three sets of refractive indices
292 and three shape distributions (spheres, spheroids, and ellipsoids) for each. We have
293 completed seven of these simulations that include the radiative effects of dust and sea salt
294 aerosols (see Table 1), as well as an additional baseline simulation in which the aerosols
295 were not radiatively active in the model (our "No Forcing" run). For each simulation the
296 model is initialized with zero aerosol mass concentration beginning in model year 2003.
297 The model is run for the period 2003 – 2050, discarding the results from 2003 – 2010 as
298 simulation spin-up (i.e., we analyze the results only for the 40 year period 2011 – 2050).
299 For all of our simulations we maintain present-day concentrations of greenhouse gases and

300 solar forcing. We use an annually repeating sea surface temperature database based on a
301 climatology of sea surface temperatures from El Nino-neutral years (Hurwitz et al., 2011).
302 The model is run at 2° x 2.5° horizontal resolution with 72 vertical sigma layers from the
303 surface to about 85 km altitude. A total of 16 aerosol tracers are carried (eight for dust and
304 eight for sea salt). The dynamical and chemical timesteps were 1800 seconds.
305
306 **3. Results**
307 **3.1. Dust Emissions**
308 Figure 3 shows the climatological global annual mean dust emission magnitude of each of
309 our simulations. The mean dust emission magnitude across our simulations is about 2100
310 – 2200 Tg yr^{-1}. There is considerable interannual variability, and the overall range is
311 between about 1900 – 2400 Tg yr^{-1}. Emissions are generally the lowest for the No Forcing
312 simulation. Highest emissions are for the simulations using the OPAC refractive indices,
313 following by the SF simulations, and finally the OBS simulations, which have similar
314 emission magnitude to the No Forcing case. Shape has a minor impact on the simulation
315 mean emissions compared to refractive index. The climatological annual mean and
316 standard deviation of emissions for each simulation are presented in Table 2.
317
318 Figure 4 shows the climatological, seasonal average dust emissions from our No Forcing
319 simulation for December-January-February (DJF), March-April-May (MAM), June-July-
320 August (JJA), and September-October-November (SON) over the period 2011 – 2050.
321 Strong dust sources are evident across northern Africa, including the sources associated
322 with the Bodele Depression and Lake Chad (most active in DJF), the eastern Libyan desert,

northern Sudan, and across Mali, Mauritania, Algeria, and Western Sahara (see Prospero et al., 2002 for an environmental description of major dust source regions). Other major sources appear in northwestern India (most active in JJA), across Saudi Arabia and Iraq, and near Lake Eyre in Australia. Less intense dust emission regions include most of Australia, northern Mexico and the western United States, across Argentina and Chile, southern Africa, and more broadly across Asia and China. The Asian dust emissions appear particularly anemic in this model relative to other models (e.g., Ginoux et al., 2004). Preliminary studies with higher spatial resolution versions of the GEOS-5 modeling system (not shown here) suggest that spatial resolution is a key ingredient in determining realistic emissions from Asian dust sources because of the complex interplay of topography and surface winds in the Takla Makan and Gobi deserts in China. The coarse resolution of the topographic features in our simulations here do not develop the strong downslope wind features in these regions that drive real-world dust emissions. Some groups have attempted to correct for these deficiencies in coarse spatial resolution climate models by imposing distribution functions on the grid box mean wind speeds (e.g., Cakmur et al., 2004; Su and Toon, 2009). We do not implement such a scheme here. Despite this shortcoming over the Asian source regions, we find a higher degree of fidelity between the coarse and fine spatial resolution versions of our model for Saharan dust sources, which is in any case the globally dominant dust source (Table 2). Accordingly we focus our evaluation and analysis on Saharan dust.

Table 2. Mean aerosol budget diagnostics for our simulations, including emissions, atmospheric burden, removal rates, lifetime, and AOT. All quantities are computed globally except for North African emissions.

	North

Experiment Name	Emissions [Tg yr^{-1}][a]	African Emissions [Tg yr^{-1}]	Burden [Tg]	k_{wet} [d^{-1}]	k_{dry} [d^{-1}]	τ [d]	AOT
No Forcing	2107 ± 93	1446 ± 83	20.82 ± 0.75	0.081	0.194	3.63	0.019
OPAC-Spheres	2221 ± 86	1556 ± 78	23.10 ± 0.88	0.078	0.187	3.77	0.022
OPAC-Spheroids	2200 ± 83	1548 ± 69	23.08 ± 0.88	0.077	0.183	3.85	0.028
OPAC-Ellipsoids	2212 ± 80	1539 ± 79	23.08 ± 0.84	0.080	0.190	3.70	0.028
SF-Spheres	2161 ± 79	1504 ± 76	22.66 ± 0.82	0.078	0.185	3.80	0.021
SF-Ellipsoids	2138 ± 70	1481 ± 63	22.50 ± 0.70	0.076	0.180	3.92	0.028
OBS-Spheres	2095 ± 76	1448 ± 69	20.91 ± 0.65	0.080	0.190	3.70	0.019
OBS-Spheroids	2099 ± 87	1453 ± 78	20.93 ± 0.79	0.080	0.195	3.65	0.024

[a]The ± indicates the standard deviation.

3.2. Dust Mass Budget

In addition to summarizing emissions, Table 2 presents a summary of characteristics of the dust mass budget in each of our simulations. The multi-year annual mean atmospheric burden of dust follows a similar pattern to the emissions, with the No Forcing and OBS simulations having the lowest burden, while the OPAC and SF simulations are the highest. There is only about a 5% range in the mean annual emissions between the simulations, whereas for the burden the range is closer to about 10% (20.82 Tg for No Forcing versus 23.10 for OPAC-Spheres). The enhanced loading corresponds to a generally greater residence time in the OPAC and SF simulations compared to the No Forcing and OBS simulations (e.g., 3.63 days for No Forcing versus 3.92 days for the SF-Ellipsoids simulation). Here, residence time is defined as in Colarco et al. (2010) as the burden divided by the loss rate. For comparison, the AeroCom-Median model dust lifetime is 4.6 days (Huneeus et al., 2011) and the GEOS-4 based GOCART dust lifetime was 5.85 days (Colarco et al., 2010). Also shown are the dust wet and dry loss frequencies defined as in Colarco et al. (2010), which provide an indication of relative importance for loss processes. The wet loss rate in our simulations is in the range 0.076 – 0.081 days^{-1}, compared to 0.055 days^{-1} in our GEOS-4 simulations (Colarco et al., 2010) and 0.084 days^{-1} for the median of

366 the AeroCom models reported in Textor et al. (2006). The dry loss rate is in the range
367 0.180 – 0.195 $days^{-1}$ here, compared to 0.116 $days^{-1}$ for our GEOS-4 simulations and 0.245
368 $days^{-1}$ for the AeroCom mean. The discussion of the loss rates and lifetimes presented here
369 is to put our model in the context of other aerosol models, but there is clearly diversity
370 among those various models. Inter-model differences arise from different
371 parameterizations of loss processes, as well as model physics, spatial resolution, and
372 meteorology. Even with respect to comparison with our GEOS-4 simulations it is important
373 to note that the GEOS-4 results came from an older version of our modeling system that
374 was driven by meteorological reanalyses and incorporated different model physics,
375 whereas here the simulations are from a free-running climate model.
376
377 Figure 5 and Table 3 present a comparison of our climatological annual simulated dust
378 surface mass concentration to the multi-year annual mean of measurements at 22 sites.
379 The data presented are the same as shown in Huneeus et al. (2011), deriving from the long-
380 term measurements managed by the Rosenstiel School of Marine and Atmospheric Sciences
381 at the University of Miami (Prospero et al., 1989; Prospero, 1996; Arimoto et al., 1995).
382 These sites are located mainly far downwind of dust source regions, and the concentration
383 of dust is obtained from high volume air samplers by measuring aluminum concentrations
384 after collected filters are ashed in an oven (assuming aluminum content is 8% of total dust
385 mass). Figure 5 shows the comparison for our OPAC-Spheres model run, also summarized
386 in Table 3 (results for all simulations are in Table S1). Our model is well correlated in the
387 multi-year annual mean with the observations, although it generally underestimates the
388 mass in the central Pacific sites. Performance appears to be best for sites impacted by

389 Saharan dust, with discrepancies between the model and observations mostly within a
390 factor 2 – 3. For the comparisons to data presented here and elsewhere in this study it is
391 important to point out that we are comparing the model climatological fields (whether
392 monthly, seasonal, or annual) to long-term averages of the various data sets used, and that
393 we are not simulating particular events captured in those data sets.
394
395 **Table 3.** Comparison of climatological mean dust surface mass concentration from the
396 OPAC-Spheres model run to multi-year mean of measurements from Propero et al. (1989),
397 Prospero (1996), and Arimoto et al. (1995).

Site #	Site Name	Years	Lat	Lon	Elv [m]	Observed [$\mu g\ m^{-3}$]	Model [$\mu g\ m^{-3}$]
1	Cape Point, South Africa	1992 - 1996	34° 20' S	18° 28' E	249	1.78	1.82
2	Cape Grim, Tasmania	1983 - 1996	40° 40' S	144° 40' E	94	1.48	2.00
3	Mawson, Antarctica	1987 - 1996	67° 35' S	62° 30' E	20	0.10	0.11
4	Palmer Station, Antarctica	1990 - 1996	64° 46' S	64° 02' W	10	0.03	0.13
5	Yate, New Caledonia	1983 - 1985	22° 08' S	167° 00' E	0	0.17	0.22
6	Funafuti, Tuvalu	1983 - 1987	08° 30' S	179° 11' W	0	0.20	0.01
7	Nauru	1983 - 1987	00° 31' S	166° 56' E	7	0.10	0.01
8	Norfolk Island	1983 - 1997	29° 04' S	167° 58' E	0	0.84	0.39
9	Rarotonga, Cook Islands	1983 - 1994	21° 30' S	159° 45' W	0	0.10	0.11
10	American Samoa	1983 - 1996	14° 15' S	170° 34' W	42	0.16	0.03
11	Midway Island	1981 - 1997	28° 13' N	177° 20' W	0	0.72	1.20
12	Cheju, South Korea	1991 - 1995	33° 31' N	126° 28' E	70	14.14	2.91
13	Hedo, Japan	1991, 1994	26° 55' N	128° 15' E	0	8.37	1.54
14	Fanning Island	1981 - 1986	03° 53' N	159° 19' W	4	0.10	0.02
15	Enewetak Atoll	1981 - 1987	11° 19' N	162° 19' E	0	0.24	0.12
16	Ragged Point, Barbados	1984 - 1998	13° 10' N	59° 25' W	41	16.15	27.18
17	Izana, Tenerife	1987 - 1998	28° 18' N	16° 30' W	2367	30.18	74.45
18	Bermuda (East & West)	1989 - 1998	32° 16' N	64° 52' W	51	3.36	6.93
19	Mace Head, Ireland	1988 -1994	53° 19' N	09° 50' W	5	1.01	0.91
20	RSMAS – University of Miami	1989 - 1998	25° 45' N	80° 15' W	5	4.59	11.38
21	Rukomechi, Zimbabwe	Not Known	16° 00' S	29° 30' E	Unknown	10.53	0.21
22	Jabirun, N. Australia	Not Known	12° 41' S	139° 53' E	Unknown	4.03	2.98

398
399 Comparisons of our model to multi-year estimates of dust deposition from the OPAC-
400 Spheres model run are shown in Figure 6, with site locations and details for all of our
401 model runs presented in Tables S2 and S3. Again, the data are as presented and screened
402 in Huneeus et al. (2011) and are derived from measurements taken during the Sea/Air
403 Exchange field campaign (SEAREX, Prospero et al., 1989, with data as presented in Ginoux

et al., 2001), measurements presented in Mahowald et al. (2009), and the Dust Indicators and Records in Terrestrial and Marine Paleoenvironments dataset (DIRTMAP, Tegen et al., 2002; Kohfeld and Harrison, 2001). The model is generally underestimating dust deposition, particularly in the remote Pacific locations, and is overestimating in the remote regions near Antarctica, but is otherwise generally within a factor of 10 of the observations.

3.3. Dust AOT

In Figure 7 we show the climatological, seasonal average dust AOT (at 550 nm) from our No Forcing simulation. Consistent with Figure 4 we see high dust AOT associated with the Bodele Depression in northern Africa peaking in DJF, the strong dust sources in western India peaking in JJA, and the peak of the Asian dust emissions during MAM. The most evident feature remote from the source regions is the Saharan dust plume over the North Atlantic Ocean. This plume moves north and south with the seasonal progression of the inter-tropical convergence zone (ITCZ), with the peak of both its northward and westward transport occurring during JJA.

Figure 8 shows a comparison of our model 550 nm dust AOT over the northern Atlantic Ocean to observations retrieved by the Multi-angle Imaging Spectroradiometer (MISR) flying onboard the NASA Terra spacecraft. MISR measures reflected radiation in four visible channels from nine different cameras viewing the same scene at different angles as the spacecraft flies over. These 36 pieces of information permit cloud clearing and selection of an appropriate lookup table of aerosol radiative properties to retrieve AOT, among other aerosol characterization capabilities (Kahn et al., 2005). Since our model is

not simulating the actual period of MISR observations we compare here our JJA model climatological dust AOT to the JJA climatology of MISR AOT for the period 2000 – 2011. For contrast with Figure 7, we show in Figure 8 the simulated dust AOT from both our No Forcing and our OPAC-Spheres model runs. Comparing these we clearly see the higher AOT in the OPAC-Spheres run consistent with higher dust emissions, as well as a further westward transport of the dust plume over the Caribbean. In comparison to MISR, the OPAC-Spheres model run has a similar north-south placement of the dust plume, although the model AOT appears somewhat higher than the observations over the source regions. The MISR observations are additionally sensitive to other aerosols besides dust, as is evident in the pollution plume along the U.S. east coast and the features associated with biomass burning in South America and southern Africa.

Figure 9 shows the climatological JJA simulated 550 nm dust AOT for each of our simulations at four different longitudes west of northern Africa. Also shown is the 2002 – 2011 JJA climatology of the 550 nm AOT from the Moderate Resolution Imaging Spectroradiometer (MODIS) onboard the NASA Aqua spacecraft. MODIS retrieves over ocean AOT in cloud-free conditions from measurements of reflected radiation at six visible channels (Tanré et al., 1997). Similar to the MISR observations shown, we are not attempting to separate the dust AOT from the total AOT in the MODIS observations, but rather focusing on what the observations tell us qualitatively about our simulations. Near the source region (the slice at 20° W) the different simulations all have a peak in the dust AOT at about 20° N, consistent with the placement of the peak in the MODIS AOT. AOT is highest for the OPAC based simulations using non-spherical optics, consistent with the

450 higher emissions in these simulations (Figure 3) and the enhanced mass extinction
451 efficiency of the non-spherical optics (Figure 2). The north-south placement of the dust
452 plume is similar for all of the model simulations, and consistent with the peak in the MODIS
453 AOT out to 60° W. By 80° W this similarity with the MODIS observations has broken down.
454 As the plume moves to the west the No Forcing and OBS based simulations (i.e., the least
455 absorbing simulations) peak in AOT more toward the southern edge of the dust plume,
456 while the OPAC and SF based simulations maintain a more uniform north-south
457 distribution and higher AOT magnitude.
458
459 Figure 10 shows the climatological JJA simulated 550 nm dust AOT for each of our
460 simulations across the North Atlantic Ocean averaged in the latitude band 10° - 30° N. For
461 comparison we also show the JJA MODIS Aqua over ocean total AOT averaged over the
462 period 2002 – 2011. In Figure 10a the results are plotted exactly according to the model
463 output, and the difference in the model simulations due to optical assumptions and
464 differences in emissions is clearly evident at the eastern longitudes, closest to the source
465 regions. In Figure 10b the model and MODIS AOT are normalized to the same value of AOT
466 at the longitude of Cape Verde (off the west coast of northern Africa, near the source
467 region, see Figure 8) and the results are plotted on a log-y axis. This emphasizes the
468 differences in the long-range transport of the dust from northern Africa, across the Atlantic,
469 and into the Caribbean, showing that in a relative sense dust is transported further west in
470 the OPAC and SF based simulations, while the OBS and No Forcing simulations are more
471 similar with the least westward export of the dust plume. Also evident is that the relative
472 westward transport of the dust plume is largely insensitive to the shape assumptions, with

473 the model results most clearly clustered according to refractive index in Figure 10b. The
474 MODIS observations lend some context, showing the diminishment of AOT as the plume
475 propagates west of Africa, although clearly the model results fall off more rapidly than the
476 satellite observations suggest. This could be due to too aggressive removal of aerosol in the
477 model. Alternatively, the MODIS observations of course also include aerosols other than
478 dust, which become an important component of the total AOT in the westernmost
479 longitudes (see Figure 8b).
480
481 Figure 11 shows a comparison of the climatological monthly mean 550 nm dust AOT from
482 each of our simulations compared to climatological monthly averaged observations from
483 the Aerosol Robotic Network (AERONET) of sun/sky scanning photometers (Holben et al.,
484 1998). AERONET observes attenuation of the direct solar beam in measuring AOT at a
485 number of wavelengths, here interpolated to 550 nm wavelength. The AERONET site
486 locations chosen are shown in Figure 8 and described in Table 4, which also shows the
487 years and total number of monthly mean AOT values being used in Figure 11. Near the
488 source region (Santa Cruz, Dahkla, Cape Verde, and Tamanrasset) the model has a similar
489 seasonal cycle to the observed AOT, although the model tends to have a higher magnitude
490 AOT relative to the observations, especially at Dahkla and Santa Cruz. At Tamanrasset the
491 simulated AOT is more comparable to the magnitude in the observations, although the
492 seasonal cycle in the model is distinctly bimodal in all simulations while it is relatively flat
493 between March and September in the observations. On the other hand, the seasonal cycle
494 and magnitude are best simulated at Cape Verde, which is directly below the main
495 summertime transport pathway.

Table 4. Description of AERONET sites used in this study. Included are the responsible principle investigator (PI) at each site, the years active, the latitude (Lat), longitude (Lon), and elevation (Elv). Also indicated are the number of monthly mean AOT values used in constructing Figure 11 (n_{aot}) and the number of JJA monthly mean inversions used in constructing the seasonal particle size distributions shown in Figure 12 (n_{inv}).

Site	PI	Years	Lat	Lon	Elv [m]	n_{aot}	n_{inv}
Ragged Point	Joe Prospero	2007 – 2011	13° 09' N	59° 25' W	40	52	11
La Parguera	Brent Holben	2000 – 2011	17° 58' N	67° 02' W	12	110	24
Bermuda	Brent Holben	1996 – 2002	32° 22 N	64° 41 W	10	64	10
Cape Verde	Didier Tanre	1994 – 2011	16° 43' N	22° 56' W	60	179	39
Santa Cruz	Emilio Cueva-Agullo	2005 – 2011	28° 28' N	16° 14 W	52	72	17
Dahkla	Hammad Benchekroun	2002 – 2003	23° 43' N	15° 56' W	12	22	6
Tamanrasset	Emilio Cueva-Agullo	2006 – 2009	22° 47' N	5° 31' E	1377	24	6

Figure 11 also shows several sites impacted on the western edge of the dust plume (Bermuda, La Parguera, and Ragged Point). Bermuda is only marginally impacted by dust, as evidenced by the relatively high Angstrom parameters at that site (not shown). There is a clear difference here again between the No Forcing and OBS based simulations on the one hand and the OPAC and SF simulations on the other, showing the more pronounced northward transport in the OPAC and SF simulations while the No Forcing and OBS based simulations have a pronounced minimum in AOT during the summer months. At La Parguera the summertime Angstrom parameter is generally low, indicative of dust, and the seasonal peak in dust AOT magnitude in June and July is well representing in the model, although the model appears to shift the peak toward the earlier part of the season. Again, the distinction between the more absorbing SF and OPAC simulations versus the No Forcing and OBS simulations is clear, with much lower AOT in the latter set. This remains the case at Ragged Point, the furthest south site considered, where again the seasonal cycle and peak AOT magnitude are well represented by the model. At all three sites we compare the ratio of the June climatological simulated dust AOT between the SF-Spheroids and No

Forcing simulations. The ratio is highest Bermuda (1.78), intermediate at La Parguera (1.59), lowest at Ragged Point (1.34). This indicates a relative preference for southward transport of the dust plume in the No Forcing model, which is also the case for the OBS based models. Incidentally, this ratio is lower than the Ragged Point value at all the near-source sites except Tamanrasset (where it is 1.44).

3.4. Dust Particle Size Distribution

Figure 12 shows a comparison of the volume dust particle size distribution simulated in the model to the retrieved particle size distribution from the AERONET measurements. Under high AOT (> 0.4) and homogeneous sky conditions AERONET can invert column integrated particle size distribution from its almucantar scan (Dubovik et al., 2000). For each of the sites shown we aggregated monthly mean particle size distributions from the AERONET dataset during JJA (the number of individual months used at each site is indicated in Table 4). For comparison we show the climatological JJA column integrated particle size distribution from the model. Note that the AERONET retrievals all contain a fine mode component to the total particle size distribution (radius < 0.5 um) that is absent in the model. This fine mode presumably corresponds to aerosols not simulated in the model. Near the source regions (Cape Verde and Tamanrasset) there is very little difference in the particle size distribution among the model runs. The model tends to peak in volume at radius ~ 1.5 um while the AERONET retrievals put the volume peak between about 2 – 3 um radius. Farther from the source regions (La Parguera and Ragged Point) the peak in the simulated particle size distribution volume occurs in the same size bin as near the sources. However, larger particles, preferentially removed by sedimentation in the model, are

541 relatively depleted compared to the retrievals at these distant sites. There are as well
542 larger differences between the model simulations at these sites, owing to greater difference
543 in the total loading at these sites.
544
545 **3.5. Dust Vertical Profiles**
546 Figure 13 shows a composite of the climatological JJA dust vertical profile from three of our
547 model simulations at four longitudes west of northern Africa. The dust vertical profile is
548 presented as the profile of the total dust mass mixing ratio. Also shown is the JJA 2011
549 aerosol attenuated backscatter profile measured by the Cloud-Aerosol Lidar with
550 Orthogonal Polarization (CALIOP) flying aboard the NASA CALIPSO spacecraft. CALIPSO
551 flies in a polar orbit in formation with the NASA Aqua spacecraft as part of the so-called "A-
552 Train" of satellites. CALIOP profiles the atmosphere with a two-channel lidar system,
553 measuring attenuated backscatter at 532 and 1064 nm and depolarization at 532 nm
554 (Winker et al., 2010). The comparison of the model vertical profile to the CALIOP
555 observations should be understood to be qualitative, as only a single season of the CALIOP
556 observations are presented, and of course the CALIOP backscatter observations are
557 sensitive to the presence of clouds and other aerosols besides dust. Still, the dust features
558 seen in the CALIOP observations are fairly typical of the observed profiles, showing an
559 elevated aerosol layer near the African coast (20° W) between about 850 – 550 hPa altitude
560 and between about 10° - 25° N latitude. This is similar to the vertical placement of the
561 aerosol plume in the model simulations shown, which peaks at about 20° N latitude and
562 between about 850 – 700 hPa altitude. As the aerosol moves west the elevated dust plume
563 is still evident in the CALIOP observations at 40° W at nearly the same latitudes, although

564 in the model the plume has moved south to a centroid of around 15° N latitude. Further
565 west the aerosol layer is less distinct in the CALIOP observations and essentially merges
566 with boundary layer aerosols. The simulated profile descends further toward the west, and
567 it becomes evident that the dust retains its elevation more clearly in the OPAC-Spheroids
568 simulation while in the OBS-Spheroids and No Forcing simulations it is at a lower altitude.
569
570 Figure 14 shows the northern Atlantic JJA climatological dust median altitude (the altitude
571 at which half the dust column mass is above and below) for each of our simulations. This
572 approach normalizes differences in the absolute column loading between the simulations.
573 Over the dust source region, where aerosol mass is well mixed by the deep boundary layer,
574 there is little difference between the simulations. When the dust is advected over the
575 ocean, however, the differences in the simulations are immediately apparent, with the
576 OPAC and SF simulations maintaining a much higher dust median altitude than either the
577 OBS or No Forcing simulations. The difference in the median altitude is about 100 hPa
578 between the SF and No Forcing simulations at about 60° W. These results are consistent
579 with what is shown in Figure 13 and suggest an explanation for the higher AOT maintained
580 by the SF and OPAC simulations across the Atlantic as shown in Figure 10: the relatively
581 higher in altitude the dust mass remains during transport, the longer its atmospheric
582 residence time and hence the further west it may be transported.
583
584 **4. Discussion**
585 **4.1. Summary of model results**

586 In Section 3 we presented our simulations of the dust aerosol lifecycle using the CARMA
587 aerosol module run online in GEOS-5. Model results were shown for the 40-year period
588 2011 – 2050 under conditions of a repeating annual cycle of sea surface temperatures
589 taken from an El Nino neutral climatology. A baseline simulation had aerosol radiative
590 interaction turned off in the model. In all other simulations dust radiative interaction with
591 the AGCM was considered, with assumptions about dust optical refractive index and shape
592 distribution varied between the simulations.
593
594 For all simulations the climatological global, annual mean dust emissions were in the range
595 of 2095 – 2221 Tg yr^{-1} (Table 2). North African dust emissions were in the range 1446 –
596 1556 Tg yr^{-1}. The difference between the high and low mean emissions are thus about 6%.
597 Our emissions are similar in magnitude to the multi-year simulations presented in the
598 GEOS-4 based version of our modeling system that employed essentially the same dust
599 mobilization scheme (Colarco et al., 2010). There the multi-year average dust emissions
600 over the same particle size range were 1970 Tg yr^{-1}. The global, annual mean dust aerosol
601 burden here is in the range 20.8 – 23.1 Tg. This is less than the burden of 31.6 Tg found in
602 Colarco et al. (2010), and the aerosol residence time is correspondingly found to be shorter
603 in the present study (3.63 – 3.92 days) than in the previous one (5.85 days). There are
604 important differences between the GEOS-5 based model and the GEOS-4 system: the
605 physical parameterizations for turbulence, convection, and precipitation are entirely
606 different, which have significant impacts on the aerosol transport and removal, and the
607 GEOS-4 simulations were run with assimilated meteorology, whereas here we are running
608 climate simulations. The shorter dust aerosol atmospheric residence time and lower dust

609 burden here are more consistent with the mean of models participating in the Aerosol
610 Comparisons between Models and Observations (AeroCom) project (19.2 Tg and 4.22 days,
611 respectively, see Textor et al., 2006; see also the updated values of 15.8 Tg and 4.6 days,
612 respectively, in Huneeus et al., 2011). Climatological annual mean dust surface mass
613 concentrations were within a factor of 3 of multi-year observations for sites impacted
614 primarily by long-range transport of Saharan dust. At remote sites in the Pacific the model
615 tended toward underestimating the observed values (Figure 5). The model tends to
616 underestimate deposition at sites impacted by Saharan dust (Figure 6), albeit mostly within
617 a factor of 3 – 5, but overestimates deposition at Antarctic sites, although the fluxes are
618 quite low.
619
620 Despite similarities in the dust emissions, burden, and lifetime, there is a wide range in the
621 value of the global, annual mean dust AOT in our simulations (range is 0.019 – 0.028). The
622 higher dust AOT values are associated with the model runs that incorporated non-spherical
623 dust optics, owing to the higher visible wavelength mass extinction efficiency (i.e., AOT per
624 unit mass) in the non-spherical cases (see Figure 2). The various simulations show similar
625 AOT spatial and temporal variability as satellite and ground-based observations (see
626 Figures 8 – 11), although there a tendency of the model AOT to be somewhat higher in
627 magnitude than the observations, particularly near the Saharan dust sources. Differences
628 in the particle size distribution are manifest mainly as differences in the loading (Figure
629 12) with a generally similar modal radius and width of the size distribution among the
630 various simulations. The vertical distribution of dust downwind of the Sahara differs
631 significantly among the simulations, with similar altitudes of the dust plume near the

continental sources (Figure 13) but a clear differentiation during westward transport (Figure 14). Median dust altitude is lowest for No Forcing simulation and only slightly higher for the OBS simulations, while the SF and OPAC simulations instead have distinctly higher dust median altitude.

Consistent with the vertical distribution discussed above, the east-west gradient in dust AOT across the Atlantic is more moderate in the OPAC and SF simulations than for the OBS and No Forcing runs (Figure 10b). This gradient is not as moderate as the MODIS observations, suggesting that removal mechanisms in the model may be somewhat overestimated. Previous studies with our model have investigated the east-west gradient of dust AOT across the Atlantic and determined wet removal was too aggressive (Nowottnick et al., 2011). While we adopted Nowottnick et al.'s (2011) suggested changes to the scavenging parameters in these simulations it seems this issue is persistent. There are differences between this study and the Nowottnick et al. (2011): their results were from a single seasonal simulation of a higher resolution run of the model driven by assimilated meteorology. Nevertheless, the more moderate east-west gradient in AOT, the higher transport altitude, and the more northward shift of the dust plume in the OPAC and SF simulations suggest they agree better with the AERONET observations (Figure 11) than do the OBS and No Forcing simulations, and thus provide the most realistic simulation.

4.2. Dust Radiative Forcing

We extend the analysis of the simulated dust AOT to encompass the dust direct radiative effect on the climate in GEOS-5. Our instantaneous forcing follows the presentation in

Randles et al. (2013), and is calculated as the net (positive down) flux change at the top of atmosphere (TOA) with and without aerosols, holding the atmospheric state fixed between two separate calls to the radiative transfer module. Defined this way, a positive TOA forcing indicates the addition of energy to the climate system (i.e., a radiative warming effect), while a negative forcing indicates a net energy loss (i.e., a radiative cooling effect). Table 5 summarizes the climatological JJA global clear-sky aerosol radiative effect in our simulations (the global, annual mean climatological values are presented in Table S4).

Table 5. Global, climatological JJA clear-sky aerosol radiative effect over ocean (land) [W m^{-2}].

	SW TOA	SW ATM	SW SFC	LW TOA	LW ATM	LW SFC	TOT ATM
OPAC-Spheres	-1.62 (-0.01)	1.04 (4.44)	-2.66 (-4.45)	0.22 (0.55)	-1.08 (-1.49)	1.30 (2.04)	-0.04 (2.95)
OPAC-Spheroids	-1.78 (0.07)	1.26 (5.29)	-3.04 (-5.22)	0.22 (0.53)	-1.07 (-1.46)	1.29 (1.98)	0.20 (3.83)
OPAC-Ellipsoids	-1.66 (-0.03)	1.11 (4.71)	-2.76 (-4.74)	0.22 (0.53)	-1.07 (-1.47)	1.29 (1.99)	0.04 (3.24)
SF-Spheres	-1.46 (0.62)	1.20 (5.22)	-2.66 (-4.60)	0.17 (0.25)	-0.96 (-0.80)	1.14 (1.05)	0.23 (4.41)
SF-Ellipsoids	-1.49 (0.57)	1.26 (5.42)	-2.75 (-4.84)	0.17 (0.22)	-0.95 (-0.74)	1.12 (0.96)	0.31 (4.67)
OBS-Spheres	-1.49 (-0.60)	0.49 (2.12)	-1.98 (-2.72)	0.16 (0.22)	-0.96 (-0.75)	1.13 (0.97)	-0.48 (1.37)
OBS-Spheroids	-1.50 (-0.54)	0.58 (2.56)	-2.09 (-3.10)	0.16 (0.20)	-0.95 (-0.70)	1.11 (0.90)	-0.37 (1.86)

Table 5 indicates a net clear-sky TOA SW cooling over the oceans for all simulations. Over land the picture is somewhat more complicated, depending on the dust optical model chosen. The weakly absorbing OBS models also exert a SW TOA clear-sky cooling over land, while the more strongly absorbing SF models exert a warming. The OPAC models have nearly zero net TOA effect over land. Figure 15 shows the climatological, JJA TOA "forcing efficiency" (forcing per unit AOT) for several of our model runs over northern Africa and the North Atlantic Ocean. Note that we show forcing efficiency in Figure 15 to facilitate comparison of the simulations, but that absolute forcing values are shown in Tables 5 and S4. So, for example, we show the forcing efficiencies for our SF-Spheres and OPAC-Spheres cases, as well as the difference between them (SF-Spheres minus OPAC-

676 Spheres). For both simulations there is the negative forcing efficiency over the ocean and
677 positive forcing efficiency over the dust source regions, and the difference plot is consistent
678 with the values in Table 5.
679
680 Also shown in Figure 15 is the shape effect, presented as the difference of the OPAC-
681 Ellipsoids and OPAC-Spheroids models relative to the OPAC-Spheres baseline. The non-
682 spherical optical models are relatively cooling at TOA over the source region compared to
683 the spherical model, but are somewhat less cooling over the oceans or land remote from
684 the source regions (positive differences in Figure 15). The presentation in Figure 15 is not
685 obviously consistent with the values in Table 5, but we remind that we are presenting
686 global mean absolute forcing in Table 5, while it is forcing efficiency shown in Figure 15.
687
688 Finally, in Figure 15 we also show the difference of the OBS-Spheres model compared to
689 the OPAC-Spheres baseline. Here the OBS-Spheres model is shown to more efficiently
690 cooling over both and land and ocean, although there is a warming feature over the
691 southern portion of the dust plume, consistent with the relatively more southward
692 transport of the dust in the OBS-Spheres model run (see Figure9).
693
694 The dust clear-sky longwave TOA effect is warming for all simulations, as shown in Table 5.
695 The global average warming over ocean is relatively small and similar for all simulations, in
696 the range of 0.16 – 0.22 W m^{-2}. Over land the effect is larger and more varied, between 0.20
697 – 0.55 W m^{-2}. The strongest longwave effect is for the OPAC based simulations, while the SF
698 and OBS simulations are more similar. Recall that the OBS and SF simulations used the

699 same refractive indices in the longwave. Figure 2 shows the relatively higher longwave
700 AOT and lower single scattering albedo for the OPAC refractive indices compared to the
701 other simulations, hence the stronger longwave effect.
702
703 Surface effects are consistent among the simulations, with an overall cooling in the
704 shortwave and warming in the longwave, and a greater magnitude for both over land than
705 ocean.
706
707 The atmospheric forcing is the difference between the TOA and surface terms in Table 5,
708 and is the amount of energy added or subtracted from the atmosphere due to the dust
709 radiative effects. Here the distinction between the different refractive index sets becomes
710 clear, with the OBS simulations having total forcing in the range -0.37 to -0.48 W m^{-2} over
711 ocean and 1.37 – 1.86 W m^{-2} over land. These can be compared to the relatively warmer
712 atmospheric forcing in the OPAC (-0.04 to 0.20 W m-2 over ocean, 2.95 – 3.83 W m^{-2} over
713 land) and the SF (0.04 – 0.23 W m^{-2} over ocean, 4.41 – 4.67 W m^{-2} over land) simulations.
714 The SF simulations have overall the greatest atmospheric direct effect, owing to their
715 weaker longwave atmospheric cooling.
716
717 Differences in the direct radiative effect among the simulations due to particle shape are
718 not clear in the longwave, although there is some consistency among them in the
719 shortwave. The spheroidal simulations have relatively stronger shortwave TOA and
720 surface cooling over and ocean compared to the associated spherical simulations, are
721 slightly more warming over land, and have relatively greater atmospheric absorption. The

ellipsoidal simulations also indicate a stronger atmospheric forcing than the spherical simulations, albeit a smaller effect than for the spheroidal models. The ellipsoids also have slightly higher TOA cooling over ocean and in contrast with the spheroids are also relatively cooling over land.

4.3. Dynamical Impact of Dust Heating

The radiative forcing of dust feeds back onto the dynamics of the GEOS-5 model. An obvious feedback is on the cycle of dust mobilization itself. For example, as Figure 3 and Table 2 illustrates there is an impact of the dust optical properties on both the magnitude and interannual variability in dust emissions. Emissions were found to be on average lowest for the No Forcing simulation and then increasing in magnitude for the OBS, SF, and then OPAC based simulations. This result is in contrast to previous studies that found decreasing dust emissions for more absorbing dust aerosols (e.g., Perlwitz and Miller, 2001; Miller et al., 2004). The emissions magnitude was more related to the refractive index choice than particle shape, a grouping made clearer in the total atmospheric forcing column of Table 5 (TOT ATM = SW ATM + LW ATM). Dust atmospheric forcing is highest for the SF simulations and lowest for the OBS simulations, with OPAC slightly less than the SF simulations.

Figure 16 shows the JJA climatological difference in the 10-m winds between the OPAC-Spheres and No Forcing model runs, as well as for the OBS-Spheres and No Forcing model runs. The general pattern is for an enhancement in the climatological mean wind field near the southern edge of the Sahara for the simulations that include dust radiative forcing

745 relative to the No Forcing simulation. The band of higher mean wind speed extends across
746 the western half of the continent between about 15° – 20° N, and is partially offset by
747 relatively weaker winds in the dust forcing simulations to the north. The wind vectors
748 shown in Figure 16 indicate this enhanced wind speed across the southern Sahara is
749 generally an onshore flow pattern, resulting from enhanced heating over land due to dust
750 relative to the fixed (cooler) sea surface temperature immediately offshore. This is
751 consistent with the previous study of Lau et al. (2009).
752
753 Also shown in Figure 16 are the JJA climatological differences in dust emissions between
754 the two simulation pairs. Emissions are the convolution of the surface wind speeds with
755 the dust source function (the thin contours in Figure 16, see also Equation 1). The region of
756 enhanced surface winds are correlated with relatively enhanced dust emissions in the dust
757 forcing simulations. This relationship is not perfect as the mean wind speeds do not tell the
758 whole story: although the mean wind speed difference is small or even negative to the
759 north of this band there are still generally enhanced emissions in this region, especially in
760 the OPAC-Spheres simulation. Because of the near cubic dependence of the emissions on
761 the surface wind speed, emissions are sensitive to the distribution of wind speeds rather
762 than simply to the mean.
763
764 Figure 17 presents a complementary look at the dynamics of this system. Here we show
765 the JJA climatological mean difference in the vertical profile of atmospheric temperature for
766 the same two pairs of simulations. The profile is the zonal mean between 15° W and 0°
767 longitude (the westernmost portion of the dust source region). Also shown is the

768 difference in the zonal mean wind speed between the forcing and No Forcing simulations
769 (thin solid and dashed contours) and the isosurface of dust concentrations exceeding 100
770 μg m^{-3} in dust concentration (thick contour line). For both pairs of simulations the
771 presence of dust acts to heat the atmosphere between about 800 - 600 hPa altitude.
772 Attenuation of incident shortwave radiation leads to a cooling under the dust plume, while
773 longwave cooling at the top of the dust layer leads to a cooling between about 500 - 400
774 hPa altitude. This temperature signal is present in both pairs of simulations, although the
775 signal has much higher amplitude in the OPAC-Spheres simulation, which has considerably
776 greater atmospheric forcing and surface cooling than the OBS-Spheres simulation (Table
777 5). The modified temperature profile in the dust forcing simulations alters the zonal winds,
778 adding a westerly component at the surface but strengthening the easterly jet aloft (by
779 about 2.5 m s^{-1} for the OPAC simulations), with the peak increase in the easterly winds at
780 about 550 hPa altitude on the southern side of the dust plume. This result is consistent
781 with the findings in Kim et al. (2010), who used a GCM with climatological aerosols to
782 identify a strengthening of the African easterly jet south of Saharan air layer resulting from
783 thermal wind balance with the addition of dust heating.
784
785 Figure 18 puts the dust heating effect into its global context. Here we show the JJA
786 climatological zonal winds and mean meridional circulation (MMC) for our No Forcing
787 simulation (contours), as well as the difference (shading) between our dust forcing
788 simulations (again, OPAC-Spheres and OBS-Spheres) and the No Forcing model run. For
789 the zonal mean wind, the signals seen in Figure 18 are similar to those shown for natural
790 aerosols in Randles et al. (2013), who used a somewhat older version of our aerosol

791 modeling system (their Figure 7h). For both of our dust forcing simulations shown here,
792 there is the enhancement in the mid-tropospheric easterly wind speed in the main Saharan
793 dust plume (between 700 and 500 hPa and 0° to 30° N, similar to Figure 17). There is as
794 well a strengthening and slight poleward shift of the southern hemisphere jet stream (at
795 200 hPa and 30° S). Both of these signals are stronger in magnitude in the OPAC-Spheres
796 simulation than the OBS-Spheres. There is also an enhancement of the westerlies at about
797 60° S, which is similar in magnitude and structure for both pairs of our simulations. As this
798 is a mostly dust-free environment this enhancement is likely due to the sea salt aerosols,
799 which were very similar in all simulations (but not radiatively coupled in the No Forcing
800 simulation). Note that the southern hemisphere enhancement in the westerlies is stronger
801 in Randles et al. (2013), who also had a significant high bias in sea salt AOT that has largely
802 been corrected in our model.
803
804 Figure 18 also shows the mean meridional circulation, a representation of the meridional-
805 vertical mass stream function. The contours in Figure 18 show the sign of the MMC for the
806 No Forcing simulation, with the arrows giving the sense and qualitative magnitude of the
807 associated vertical motion. The effect of the aerosol forcing is to strengthen both the
808 northern and southern branches of the Hadley cell, enhancing both the upward motion on
809 the equatorward side of the cells and the downward motion on the poleward side. The
810 perturbations suggest a slightly northward shift in the cell's positions, supported also by a
811 northward shift of the ITCZ evident in the modeled precipitation fields (not shown), similar
812 to Wilcox et al. (2010). Again, the strengthening and the shift are more pronounced for the
813 OPAC-Spheres simulation than the OBS-Spheres case.

The results for the MMC are somewhat at odds with Randles et al. (2013), who diagnosed a summertime weakening of the MMC due to natural aerosols, but there are some significant differences between their simulations and ours. For one, they had a much higher baseline forcing due to high sea salt AOT (noted above). Additionally, they had annually varying SSTs, while we are using a fixed, repeating cycle of SSTs. Finally, their shortwave dust forcing was weak compared to the OPAC-Spheres model, more like what is shown in the OBS-Spheres, which has a weaker impact overall. On the other hand, the Randles et al. (2013) were broadly consistent with Allen and Sherwood (2010) who showed a similar weakening of the JJA Hadley cell due to dust and sea salt for climate model simulations with imposed (not dynamic) aerosol concentrations and fixed SSTs. Our results for the MMC, by contrast, are more like what Randles et al. (2013) and Allen and Sherwood (2010) show for anthropogenic aerosols, strengthening the Hadley cells. The anthropogenic aerosols in those studies are typically quite absorbing in the shortwave, in contrast to our OBS-Spheres simulations but more like our OPAC-Spheres model run.

5. Conclusions

The discussion above suggests several general conclusions of our study. First, we find that higher Saharan dust emissions are associated with increasing the radiative impact of the dust. Table 5 shows greatest overall atmospheric heating for the SF based simulations, followed by the OPAC and the OBS based simulations. Dust emissions are similar, highest for the OPAC simulations, lower for the SF runs, and lowest for the OBS and No Forcing simulations (Figure 3 and Table 2). The higher dust emissions are the result of

837 enhancement in the surface wind speeds over important dust source regions (Figure 16).
838 These results are opposite to studies by Perlwitz and Miller (2001) and Miller et al. (2004),
839 where the highest magnitude dust emissions were found for simulations in which dust was
840 a passive tracer and the lowest overall emissions were found for the most absorbing dust
841 optical models. Those studies were carried out in a relatively coarser spatial resolution
842 AGCM (4° x 5° latitude by longitude with 12 vertical layers), and the Miller et al. (2004)
843 study included a mixed-layer ocean model, so there are important differences in the overall
844 experiment construction.
845
846 Second, we find that dust is transported more efficiently and at higher altitudes in our
847 model the more absorbing the dust optical properties. Over the northern Atlantic Ocean
848 dust is transported further to the west and at a more northern latitude for our OPAC based
849 simulations when compared to the No Forcing simulation (Figures 9 and 10). Relatively
850 furthest westward transport of the summertime Saharan dust plume is in our SF based
851 simulations, while the weakly absorbing OBS based simulations are most like the No
852 Forcing case. Dust median altitude is highest for the SF and OPAC simulations, and lowest
853 for the OBS and No Forcing cases (Figure 14). The more absorbing simulations are
854 associated with a stronger easterly jet as the dust is leaving Africa (Figures 13 and 17),
855 resulting in more rapid transport and generally longer atmospheric residence times (Table
856 2). The heating by the dust has a stabilizing effect on the lowest part of the atmosphere
857 near the source region but sets up an onshore flow and strengthens the mean meridional
858 circulation associated with the Hadley cells (Figure 18). The enhancement of the upward
859 motion in the Hadley cells is associated with the peak dust concentrations and leads the

overall elevation in the dust altitude. Overall we find a better agreement between the modeled and observed dust distributions for the simulations with the higher dust absorption, leading us to recommend the OPAC or SF optical tables over the OBS tables.

Finally, the impact of particle shape is a second order effect in our simulations. Although particle nonsphericity results in a higher dust mass extinction efficiency and higher dust AOT (Table 2 and Figure 2) than for spherical properties, the character of the dust transport is more clearly group by refractive index choice (i.e., OBS vs. OPAC vs. SF) than by particle shape (Figures 10 and 14). That said, the forcing appears to be sensitive to particle shape, with particularly the spheroidal model showing > 10% higher total atmospheric forcing over land than the corresponding spherical simulations. Ellipsoidal simulations are more similar to their spherical counterparts. We stress that even if radiative effects of particle shape are relatively unimportant in the overall dust-climate interaction, as our studies here suggest, it is likely an important consideration for observation (i.e., radiance) simulation from modeled aerosol fields.

Future studies with this model would invoke several enhancements to our previous modeling capabilities. First, higher spatial resolution model runs would permit a more realistic simulation—and, hence, evaluation—of dust from Asian sources. Second, our simulations evolved very similar particle size distributions that were insensitive to the dust optics and generally underestimated coarse mode dust mass; in future simulations we would investigate alternative particle size formulations (e.g., Kok 2011) and a more thorough evaluation of the simulated particle size distribution. There is also a need to

883 evaluate model parameterizations, particular with respect to wet loss processes in
884 governing the east-west gradient of dust over the Atlantic. Likewise we could as well
885 investigate the importance of the wind speed PDF in governing dust emissions, as
886 suggested elsewhere (e.g., Cakmur et al., 2004; Su and Toon, 2009). Finally, a coupled
887 ocean model was not available in GEOS-5 at the time these simulations were performed;
888 such a capability is soon available and can be applied to these same sorts of simulations to
889 more fully explore the climate feedback as a function of dust optical properties.
890

891 **Acknowledgements**

892 The NASA Modeling, Analysis, and Prediction (MAP) program (David Considine, program
893 manager) supported this work under project 08-MAP-80. Resources supporting this work
894 were provided by the NASA High-End Computing (HEC) Program through the NASA
895 Advanced Supercomputing (NAS) Division at Ames Research Center and the NASA Center
896 for Climate Simulations (NCCS) at Goddard Space Flight Center under project SMD-11-
897 2567. We thank Arlindo da Silva for assistance in implementing the CARMA model in
898 GEOS-5.
899

900 **References**

901 Ackerman, A., Toon, O. and HOBBS, P.: A Model for Particle Microphysics, Turbulent Mixing, and Radiative-
902 Transfer in the Stratocumulus-Topped Marine Boundary-Layer and Comparisons with Measurements, J
903 Atmos Sci, 52(8), 1204–1236, 1995.

904 Allen, R. J. and Sherwood, S. C.: The impact of natural versus anthropogenic aerosols on atmospheric
905 circulation in the Community Atmosphere Model, Clim Dyn, 36(9-10), 1959–1978, doi:10.1007/s00382-
906 010-0898-8, 2010.

907 Arimoto, R., Duce, R. A., Ray, B. J., Ellis, W. G., Cullen, J. D., and Merrill, J. T.: Trace-Elements in the Atmosphere
908 over the North-Atlantic, J. Geophys. Res.-Atmos., 100(D1), 1199–1213, 1995.

909 Balkanski, Y., Schulz, M., Claquin, T. and Guibert, S.: Reevaluation of Mineral aerosol radiative forcings
910 suggests a better agreement with satellite and AERONET data, Atmos Chem Phys, 7, 81–95, 2007.

911 Bauer, S., Balkanski, Y., Schulz, M., Hauglustaine, D. and Dentener, F.: Global modeling of heterogeneous
912 chemistry on mineral aerosol surfaces: Influence on tropospheric ozone chemistry and comparison to
913 observations, J Geophys Res-Atmos, 109(D2), D02304, doi:10.1029/2003JD003868, 2004.

914 Bian, H. and Zender, C.: Mineral dust and global tropospheric chemistry: Relative roles of photolysis and
915 heterogeneous uptake, J Geophys Res-Atmos, 108(D21), 4672, doi:10.1029/2002JD003143, 2003.

916 Bian, H., P. Colarco, M. Chin, G. Chen, A.R. Douglass, J.M. Rodriguez, Q. Liang, D. Blake, D.A. Chu, A. da Silva, A.S.
917 Darmenov, G. Diskin, H.E. Fuelberg, G. Huey, Y. Kondo, J.E. Nielsen, X. Pan, and A. Wisthaler: Investigation
918 of source attributions of pollution to the western Arctic during the NASA ARCTAS field campaign, Atmos
919 Chem and Phys (submitted, 2013).

920 Cakmur, R., Miller, R. and Torres, O.: Incorporating the effect of small-scale circulations upon dust emission in
921 an atmospheric general circulation model, J Geophys Res-Atmos, 109(D7), D07201,
922 doi:10.1029/2003JD004067, 2004.

923 Chou, M. and Suarez, M. J.: An Efficient Thermal Infrared Radiation Parameterization for Use in General
924 Circulation Models, Technical Report Series on Global Modeling and Data Assimilation, 3, 1–98, 1994.

925 Chou, M. and Suarez, M. J.: A Solar Radiation Parameterization for Atmospheric Studies, Technical Report
926 Series on Global Modeling and Data Assimilation, 15, 1–51, 1999.

927 Chou, M., Suarez, M. J., Liang, X.-Z. and Yan, M. M. H.: A Thermal Infrared Radiation Parameterization for
928 Atmospheric Studies, Technical Report Series on Global Modeling and Data Assimilation, 19, 1–68, 2001.

929 Colarco, P., Da Silva, A., Chin, M. and Diehl, T.: Online simulations of global aerosol distributions in the NASA
930 GEOS-4 model and comparisons to satellite and ground-based aerosol optical depth, J Geophys Res-
931 Atmos, 115, –, doi:10.1029/2009JD012820, 2010.

932 Colarco, P., Schoeberl, M., Doddridge, B., Marufu, L., Torres, O. and Welton, E.: Transport of smoke from
933 Canadian forest fires to the surface near Washington, D. C.: Injection height, entrainment, and optical
934 properties, J Geophys Res-Atmos, 109, –, doi:10.1029/2003JD004248, 2004.

935 Colarco, P., Toon, O. and Holben, B.: Saharan dust transport to the Caribbean during PRIDE: 1. Influence of
936 dust sources and removal mechanisms on the timing and magnitude of downwind aerosol optical depth
937 events from simulations of in situ and remote sensing observations, J Geophys Res-Atmos, 108, –,
938 doi:10.1029/2002JD002658, 2003.

939 Colarco, P., Toon, O., Torres, O. and Rasch, P.: Determining the UV imaginary index of refraction of Saharan
940 dust particles from Total Ozone Mapping Spectrometer data using a three-dimensional model of dust
941 transport, J Geophys Res-Atmos, 107, –, doi:10.1029/2001JD000903, 2002.

942 Dentener, F., Carmichael, G., Zhang, Y., Lelieveld, J. and Crutzen, P.: Role of mineral aerosol as a reactive
943 surface in the global troposphere, J Geophys Res-Atmos, 101(D17), 22869–22889, 1996.

944 Dubovik, O. and King, M.: A flexible inversion algorithm for retrieval of aerosol optical properties from Sun
945 and sky radiance measurements, J Geophys Res-Atmos, 105(D16), 20673–20696, 2000.

946 Dubovik, O., Sinyuk, A., Lapyonok, T., Holben, B. N., Mishchenko, M., Yang, P., Eck, T. F., Volten, H., Muñoz, O.,
947 Veihelmann, B., van der Zande, W. J., et al.: Application of spheroid models to account for aerosol particle
948 nonsphericity in remote sensing of desert dust, J Geophys Res, 111(D11), doi:10.1029/2005JD006619,
949 2006.

950 Dunion, J. and Velden, C.: The impact of the Saharan air layer on Atlantic tropical cyclone activity, B Am
951 Meteorol Soc, 85(3), 353–+, doi:10.1175/BAMS-85-3-353, 2004.

952 English, J. M., Toon, O. B. and Mills, M. J.: Microphysical simulations of sulfur burdens from stratospheric sulfur
953 geoengineering, Atmos Chem Phys, 12(10), 4775–4793, doi:10.5194/acp-12-4775-2012, 2012.

954 English, J., Toon, O. and Mills, M.: Microphysical simulations of new particle formation in the upper
955 troposphere and lower stratosphere, Atmospheric Chemistry & …, 2011.

956 Evan, A. T., Dunion, J., Foley, J. A., Heidinger, A. K. and Velden, C. S.: New evidence for a relationship between

Atlantic tropical cyclone activity and African dust outbreaks, Geophys Res Lett, 33(19), L19813, doi:10.1029/2006GL026408, 2006.

Fan, T. and Toon, O. B.: Modeling sea-salt aerosol in a coupled climate and sectional microphysical model: mass, optical depth and number concentration, Atmos Chem Phys, 11(9), 4587–4610, doi:10.5194/acp-11-4587-2011, 2011.

Feng, Q., Yang, P., Kattawar, G. W., Hsu, C. N., Tsay, S.-C. and Laszlo, I.: Effects of particle nonsphericity and radiation polarization on retrieving dust properties from MODIS observations, J Aerosol Sci, 40(9), 776–789, doi:10.1016/j.jaerosci.2009.05.001, 2009.

Fung, I., Meyn, S., Tegen, I., Doney, S., John, J. and Bishop, J.: Iron supply and demand in the upper ocean, Global Biogeochem Cy, 14(1), 281–295, 2000.

Gerber, H. E.: Relative-Humidity Parameterization of the Navy Aerosol Model (NAM), NRL Report 8956, 1–16, 1985.

Ginoux, P.: Effects of nonsphericity on mineral dust modeling, J Geophys Res-Atmos, 108(D2), 4052, doi:10.1029/2002JD002516, 2003.

Ginoux, P., Chin, M., Tegen, I., Prospero, J., Holben, B., Dubovik, O. and Lin, S.: Sources and distributions of dust aerosols simulated with the GOCART model, J Geophys Res-Atmos, 106(D17), 20255–20273, 2001.

Ginoux, P., Prospero, J., Torres, O. and Chin, M.: Long-term simulation of global dust distribution with the GOCART model: correlation with North Atlantic Oscillation, Environ Modell Softw, 19(2), 113–128, doi:10.1016/S1364-8152(03)00114-2, 2004.

Gong, S.: A parameterization of sea-salt aerosol source function for sub- and super-micron particles, Global Biogeochem Cy, 17(4), 1097, doi:10.1029/2003GB002079, 2003.

Hess, M., Koepke, P. and Schult, I.: Optical properties of aerosols and clouds: The software package OPAC, B Am Meteorol Soc, 79(5), 831–844, 1998.

Holben, B., Eck, T., Slutsker, I., Tanre, D., Buis, J., Setzer, A., Vermote, E., Reagan, J., Kaufman, Y., Nakajima, T., Lavenu, F., et al.: AERONET - A federated instrument network and data archive for aerosol characterization, Remote Sens Environ, 66(1), 1–16, 1998.

Huneeus, N., Schulz, M., Balkanski, Y., Griesfeller, J., Prospero, J., Kinne, S., Bauer, S., Boucher, O., Chin, M., Dentener, F., Diehl, T., et al.: Global dust model intercomparison in AeroCom phase I, Atmos Chem Phys, 11(15), 7781–7816, doi:10.5194/acp-11-7781-2011, 2011.

Hurwitz, M. M., Song, I. S., Oman, L. D., Newman, P. A., Molod, A. M., Frith, S. M. and Nielsen, J. E.: Response of the Antarctic stratosphere to warm pool El Nino Events in the GEOS CCM, Atmos Chem Phys, 11(18), 9659–9669, doi:10.5194/acp-11-9659-2011, 2011.

Intergovernmental Panel on Climate Change: Climate change 2007: The physical science basis, Contribution of Working Group I to the Fourth Assessment Report of the Intergovernmental Panel on Climate Change, edited by S. Solomon et al., 996 pp., Cambridge University Press, Cambridge, United Kingdom and New York, NY, USA, 2007.

Jensen, E., Toon, O., Westphal, D., Kinne, S. and Heymsfield, A.: Microphysical Modeling of Cirrus: 1. Comparison with 1986 FIRE IFO Measurements, J Geophys Res-Atmos, 99(D5), 10421–10442, 1994.

Jickells, T., An, Z., Andersen, K., Baker, A., Bergametti, G., Brooks, N., Cao, J., Boyd, P., Duce, R., Hunter, K., Kawahata, H., et al.: Global iron connections between desert dust, ocean biogeochemistry, and climate, Science, 308(5718), 67–71, 2005.

Jones, C., Mahowald, N. and Luo, C.: Observational evidence of African desert dust intensification of easterly waves, Geophys Res Lett, 31(17), L17208, doi:10.1029/2004GL020107, 2004.

Kahn, R., Gaitley, B., Martonchik, J., Diner, D., Crean, K. and Holben, B.: Multiangle Imaging Spectroradiometer (MISR) global aerosol optical depth validation based on 2 years of coincident Aerosol Robotic Network (AERONET) observations, J Geophys Res-Atmos, 110(D10), D10S04, doi:10.1029/2004JD004706, 2005.

1003 Kaufman, Y., Tanre, D., Dubovik, O., Karnieli, A. and Remer, L.: Absorption of sunlight by dust as inferred from
1004 satellite and ground-based remote sensing, Geophys Res Lett, 28(8), 1479–1482, 2001.

1005 Kim, D., Chin, M., Yu, H., Eck, T. F., Sinyuk, A., Smirnov, A. and Holben, B. N.: Dust optical properties over North
1006 Africa and Arabian Peninsula derived from the AERONET dataset, Atmos Chem Phys, 11(20), 10733–
1007 10741, doi:10.5194/acp-11-10733-2011, 2011.

1008 Kim, K.-M., Lau, W. K. M., Sud, Y. C. and Walker, G. K.: Influence of aerosol-radiative forcings on the diurnal and
1009 seasonal cycles of rainfall over West Africa and Eastern Atlantic Ocean using GCM simulations, Clim Dyn,
1010 35(1), 115–126, doi:10.1007/s00382-010-0750-1, 2010.

1011 Kohfeld, K. E. and Harrison, S. P.: DIRTMAP: the geological record of dust, Earth-Science Reviews, 54(1-3), 81–
1012 114, doi:10.1016/S0012-8252(01)00042-3, 2001.

1013 Kok, J. F.: A scaling theory for the size distribution of emitted dust aerosols suggests climate models
1014 underestimate the size of the global dust cycle, Proceedings of the National Academy of Sciences, 108(3),
1015 1016, 2011.

1016 Koster, R., Suarez, M., Ducharne, A., Stieglitz, M. and Kumar, P.: A catchment-based approach to modeling land
1017 surface processes in a general circulation model 1. Model structure, J Geophys Res-Atmos, 105(D20),
1018 24809–24822, 2000.

1019 Lau, K. M. and Kim, K. M.: Cooling of the Atlantic by Saharan dust, Geophys Res Lett, 34,
1020 doi:10.1029/2007GL031538, 2007.

1021 Lau, K. M., Kim, K. M., Sud, Y. C. and Walker, G. K.: A GCM study of the response of the atmospheric water cycle
1022 of West Africa and the Atlantic to Saharan dust radiative forcing,, 27(10), 4023, 2009.

1023 Lin, S.: A "vertically Lagrangian'' finite-volume dynamical core for global models, Mon Weather Rev, 132(10),
1024 2293–2307, 2004.

1025 Lock, A., Brown, A., Bush, M., Martin, G. and Smith, R.: A new boundary layer mixing scheme. Part I: Scheme
1026 description and single-column model tests, Mon Weather Rev, 128(9), 3187–3199, 2000.

1027 Madry, W. L., Toon, O. B. and O'Dowd, C. D.: Modeled optical thickness of sea-salt aerosol, J Geophys Res-
1028 Atmos, 116, –, doi:10.1029/2010JD014691, 2011.

1029 Mahowald, N. M., Engelstaedter, S., Luo, C., Sealy, A., Artaxo, P., Benitez-Nelson, C., Bonnet, S., Chen, Y., Chuang,
1030 P. Y., Cohen, D. D., Dulac, F., et al.: Atmospheric Iron Deposition: Global Distribution, Variability, and
1031 Human Perturbations, Annu Rev Mar Sci, 1, 245–278, doi:10.1146/annurev.marine.010908.163727,
1032 2009.

1033 Marticorena, B. and Bergametti, G.: Modeling the Atmospheric Dust Cycle: 1. Design of a soil-derived dust
1034 emission scheme, J Geophys Res-Atmos, 100(D8), 16415–16430, 1995.

1035 Martin, J. H.: Glacial-interglacial CO 2change: The Iron Hypothesis, Paleoceanography, 5(1), 1–13,
1036 doi:10.1029/PA005i001p00001, 2010.

1037 Matichuk, R. I., Colarco, P. R., Smith, J. A. and Toon, O. B.: Modeling the transport and optical properties of
1038 smoke aerosols from African savanna fires during the Southern African Regional Science Initiative
1039 campaign (SAFARI 2000), J Geophys Res-Atmos, 112, –, doi:10.1029/2006JD007528, 2007.

1040 Matichuk, R. I., Colarco, P. R., Smith, J. A. and Toon, O. B.: Modeling the transport and optical properties of
1041 smoke plumes from South American biomass burning, J Geophys Res-Atmos, 113, –,
1042 doi:10.1029/2007JD009005, 2008.

1043 Meng, Z., Yang, P., Kattawar, G. W., Bi, L., Liou, K. N. and Laszlo, I.: Single-scattering properties of tri-axial
1044 ellipsoidal mineral dust aerosols: A database for application to radiative transfer calculations, J Aerosol
1045 Sci, 41(5), 501–512, doi:10.1016/j.jaerosci.2010.02.008, 2010.

1046 Miller, R., Tegen, I. and Perlwitz, J.: Surface radiative forcing by soil dust aerosols and the hydrologic cycle, J
1047 Geophys Res-Atmos, 109(D4), –, doi:10.1029/2003JD004085, 2004.

1048 Mishchenko,M.I., and Travis,L.D.: Capabilities and limitations of acurrent FORTRAN implementation of theT-

matrix method for randomly oriented rotationally symmetric scatterers. J Quant Spectrosc Radiat Transfer, 60, 309-324, 1998.

Mishchenko, M., Lacis, A., Carlson, B. and Travis, L.: Nonsphericity of Dust-Like Tropospheric Aerosols - Implications for Aerosol Remote-Sensing and Climate Modeling, Geophys Res Lett, 22(9), 1077–1080, 1995.

Moorthi, S. and Suarez, M.: Relaxed Arakawa-Schubert - A Parameterization of Moist Convection for General-Circulation Models, Mon Weather Rev, 120(6), 978–1002, 1992.

Moulin, C., Gordon, H., Banzon, V. and Evans, R.: Assessment of Saharan dust absorption in the visible from SeaWiFS imagery, J Geophys Res-Atmos, 106(D16), 18239–18249, 2001.

Nowottnick, E., Colarco, P., Ferrare, R., Chen, G., Ismail, S., Anderson, B. and Browell, E.: Online simulations of mineral dust aerosol distributions: Comparisons to NAMMA observations and sensitivity to dust emission parameterization, J Geophys Res-Atmos, 115, –, doi:10.1029/2009JD012692, 2010.

Nussenzveig, H.M.(1992). *Diffraction Effects in Semiclassical Scattering*. London: Cambridge University.

Ott, L., Duncan, B., Pawson, S., Colarco, P., Chin, M., Randles, C., Diehl, T. and Nielsen, E.: Influence of the 2006 Indonesian biomass burning aerosols on tropical dynamics studied with the GEOS-5 AGCM, J Geophys Res-Atmos, 115, –, doi:10.1029/2009JD013181, 2010.

Perlwitz, J., Tegen, I. and Miller, R.: Interactive soil dust aerosol model in the GISS GCM 1. Sensitivity of the soil dust cycle to radiative properties of soil dust aerosols, J Geophys Res-Atmos, 106(D16), 18167–18192, 2001.

Prospero, J. M., Uematsu, M., and Savoie, D. L.: Mineral aerosol transport to the Pacific Ocean, edited by: Riley, J. P., 187–218, Academic Press, New York, 1989.

Prospero, J. M.: The Atmospheric Transport of Particles to the Ocean, in: Particle Flux in the Ocean, edited by: Ittekkot, V., Scha¨fer, P., Honjo, S., and Depetris, P. J., John Wiley & Sons Ltd., New York, 1996.

Prospero, J.: Long-range transport of mineral dust in the global atmosphere: Impact of African dust on the environment of the southeastern United States, P Natl Acad Sci Usa, 96(7), 3396–3403, 1999.

Quijano, A., Sokolik, I. and Toon, O.: Radiative heating rates and direct radiative forcing by mineral dust in cloudy atmospheric conditions, J Geophys Res-Atmos, 105(D10), 12207–12219, 2000.

Randles, C. A., Colarco, P. R. and Da Silva, A.: Direct and semi-direct aerosol effects in the NASA GEOS-5 AGCM: Aerosol-climate interactions due to prognostic versus prescribed aerosols, J Geophys Res, doi:10.1029/2012JD018388, 2013.

Reale, O., Lau, K. M. and Da Silva, A.: Impact of an Interactive Aerosol on the African Easterly Jet in the NASA GEOS-5 Global Forecasting System, Weather and Forecasting, 26(4), 504–519, doi:10.1175/WAF-D-10-05025.1, 2011.

Rienecker, M. M., Suarez, M. J., Gelaro, R., Todling, R., Bacmeister, J., Liu, E., Bosilovich, M. G., Schubert, S. D., Takacs, L., Kim, G.-K., Bloom, S., et al.: MERRA: NASA's Modern-Era Retrospective Analysis for Research and Applications, J Climate, 24(14), 3624–3648, doi:10.1175/JCLI-D-11-00015.1, 2011.

Rienecker, M., Suarez, M., Todling, R., Bacmeister, J., Takacs, L., Liu, H.-C., Gu, W., Sienkieicz, M., Koster, R., Gelaro, R., Stajner, I., et al.: The GEOS-5 Data Assimilation System--Documentation of Version 5.0.1, 5.1.0, and 5.2.0, NASA Technical Report Series on Global Modeling and Data Assimilation, 27, 1–118, 2008.

Rosenfeld, D., Rudich, Y. and Lahav, R.: Desert dust suppressing precipitation: A possible desertification feedback loop, P Natl Acad Sci Usa, 98(11), 5975–5980, 2001.

Rothman, L. S., Gordon, I. E., Barbe, A., Benner, D. C., Bernath, P. F., Birk, M., Boudon, V., Brown, L. R., Campargue, A., Champion, J. P., Chance, K., et al.: The HITRAN 2008 molecular spectroscopic database, J Quant Spectrosc Ra, 110(9-10), 533–572, doi:10.1016/j.jqsrt.2009.02.013, 2009.

Sassen, K., DeMott, P., Prospero, J. and Poellot, M.: Saharan dust storms and indirect aerosol effects on clouds: CRYSTAL-FACE results, Geophys Res Lett, 30(12), 1633, doi:10.1029/2003GL017371, 2003.

1095 Shettle, E. and Fenn, R. W.: Models for the Aerosols of the Lower Atmosphere and the Effects of Humidity
1096 Variations on Their Optical Properties,, 1–94, 2012.

1097 Shinn, E., Smith, G., Prospero, J., Betzer, P., Hayes, M., Garrison, V. and Barber, R.: African dust and the demise
1098 of Caribbean coral reefs, Geophys Res Lett, 27(19), 3029–3032, 2000.

1099 Sinyuk, A., Torres, O. and Dubovik, O.: Combined use of satellite and surface observations to infer the
1100 imaginary part of refractive index of Saharan dust, Geophys Res Lett, 30(2), 1081,
1101 doi:10.1029/2002GL016189, 2003.

1102 Sokolik, I. and Toon, O.: Direct radiative forcing by anthropogenic airborne mineral aerosols, Nature,
1103 381(6584), 681–683, 1996.

1104 Sokolik, I. and Toon, O.: Incorporation of mineralogical composition into models of the radiative properties of
1105 mineral aerosol from UV to IR wavelengths, J Geophys Res-Atmos, 104(D8), 9423–9444, 1999.

1106 Su, L. and Toon, O. B.: Numerical simulations of Asian dust storms using a coupled climate-aerosol
1107 microphysical model, J Geophys Res-Atmos, 114, D14202, doi:10.1029/2008JD010956, 2009.

1108 Swap, R., Garstang, M., Greco, S., Talbot, R. and Kallberg, P.: Saharan dust in the Amazon Basin, Tellus B, 44(2),
1109 133–149, doi:10.1034/j.1600-0889.1992.t01-1-00005.x, 1992.

1110 Tanre, D., Kaufman, Y., Herman, M. and Mattoo, S.: Remote sensing of aerosol properties over oceans using the
1111 MODIS/EOS spectral radiances, J Geophys Res-Atmos, 102(D14), 16971–16988, 1997.

1112 Tegen, I. and FUNG, I.: MODELING OF MINERAL DUST IN THE ATMOSPHERE - SOURCES, TRANSPORT, AND
1113 OPTICAL-THICKNESS, J Geophys Res-Atmos, 99(D11), 22897–22914, 1994.

1114 Tegen, I. and Lacis, A.: Modeling of particle size distribution and its influence on the radiative properties of
1115 mineral dust aerosol, J Geophys Res-Atmos, 101(D14), 19237–19244, 1996.

1116 Tegen, I., Harrison, S., Kohfeld, K., Prentice, I., Coe, M. and Heimann, M.: Impact of vegetation and preferential
1117 source areas on global dust aerosol: Results from a model study, J Geophys Res-Atmos, 107(D21), 4576,
1118 doi:10.1029/2001JD000963, 2002.

1119 Textor, C., Schulz, M., Guibert, S., Kinne, S., Balkanski, Y., Bauer, S., Berntsen, T., Berglen, T., Boucher, O., Chin,
1120 M., Dentener, F., et al.: Analysis and quantification of the diversities of aerosol life cycles within AeroCom,
1121 Atmos Chem Phys, 6, 1777–1813, 2006.

1122 Toon, O., Turco, R., Westphal, D., Malone, R. and Liu, M.: A Multidimensional Model for Aerosols – Description
1123 of Computational Analogs, J Atmos Sci, 45(15), 2123–2143, 1988.

1124 Wilcox, E. M., Lau, K. M. and Kim, K.-M.: A northward shift of the North Atlantic Ocean Intertropical
1125 Convergence Zone in response to summertime Saharan dust outbreaks, Geophys Res Lett, 37(4), L04804,
1126 doi:10.1029/2009GL041774, 2010.

1127 Winker, D. M., Pelon, J., Coakley, J. A. J., Ackerman, S. A., Charlson, R. J., Colarco, P. R., Flamant, P., Fu, Q., Hoff, R.
1128 M., Kittaka, C., Kubar, T. L., et al.: The CALIPSO Mission: A Global 3D View of Aerosols and Clouds, B Am
1129 Meteorol Soc, 91(9), 1211–1229, doi:10.1175/2010BAMS3009.1, 2010.

1130 Wiscombe, W.: Improved Mie scattering algorithms, Appl Optics, 19(9), 1505–1509, 1980.

1131 Wong, S.: Suppression of deep convection over the tropical North Atlantic by the Saharan Air Layer, Geophys
1132 Res Lett, 32(9), L09808, doi:10.1029/2004GL022295, 2005.

1133 Yang P, Liou K. Geometric-optics—integral-equation method for light scattering by nonspherical ice crystals.
1134 Appl. Optics. 35, 6568-84, 1996.

1135 Yi, B., Hsu, C. N., Yang, P. and Tsay, S.-C.: Radiative transfer simulation of dust-like aerosols Uncertainties from
1136 particle shape and refractive index, J Aerosol Sci, 42(10), 631–644, doi:10.1016/j.jaerosci.2011.06.008,
1137 2011.

1138 Yurkin MA, Maltsev VP, Hoekstra AG. The discrete dipole approximation for simulation of light scattering by
1139 particles much larger than the wavelength. J Quant Spectrosc Radiat Trans., 106, 546–57, 2007.

Zender, C., Bian, H. and Newman, D.: Mineral Dust Entrainment and Deposition (DEAD) model: Description and 1990s dust climatology, J Geophys Res-Atmos, 108(D14), 4416, doi:10.1029/2002JD002775, 2003.

Zender, C., Miller, R. and Tegen, I.: Quantifying mineral dust mass budgets: Terminology, constraints, and current estimates, EOS, 2004.

Zhu, Y. and Gelaro, R.: Observation Sensitivity Calculations Using the Adjoint of the Gridpoint Statistical Interpolation (GSI) Analysis System, Mon Weather Rev, 136(1), 335–351, doi:10.1175/MWR3525.1, 2008.

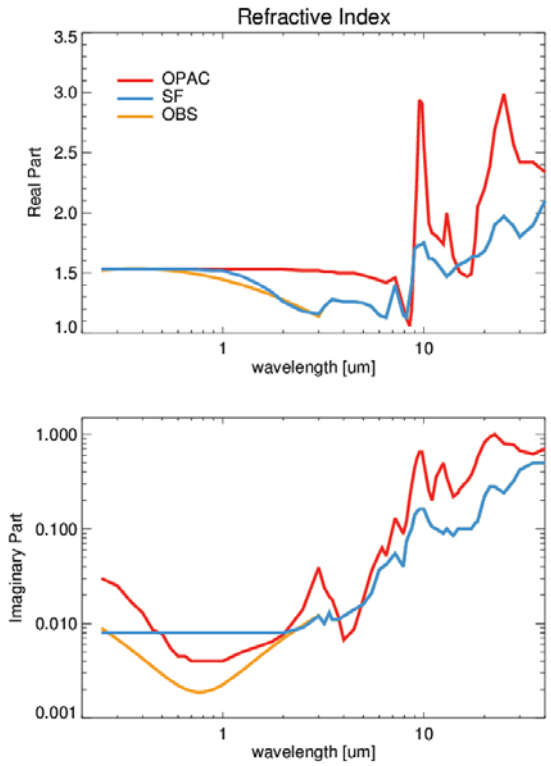

Figure 1. Spectral refractive indices used in this study for the OPAC, SF, and OBS simulations. Note that the OBS curve (the orange curve) is identical to the SF curve for wavelengths greater than 3 μm.

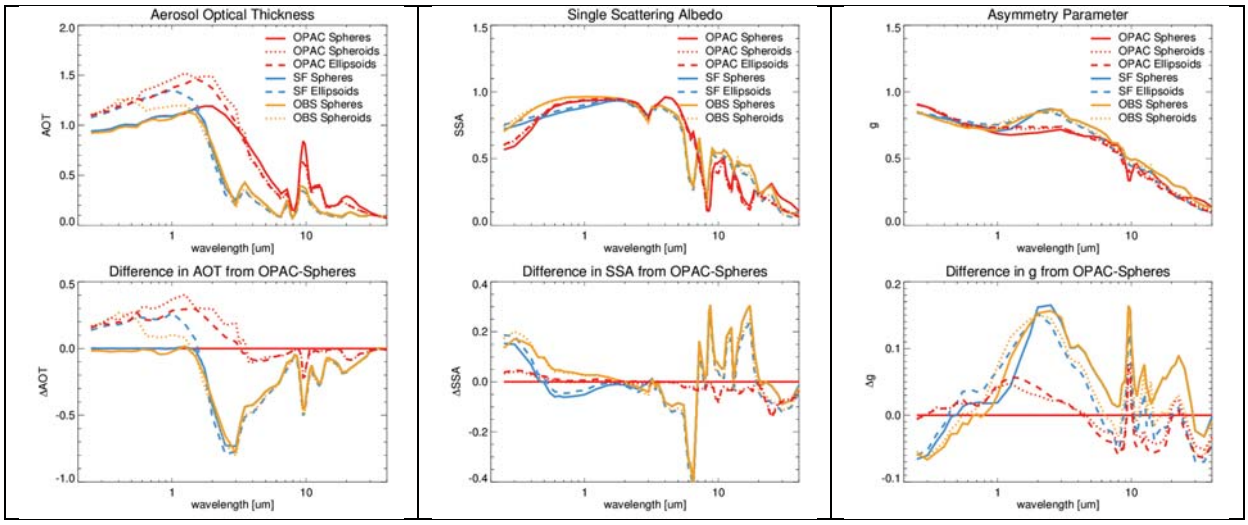

Figure 2. Spectral aerosol optical thickness (AOT, left), single scattering albedo (SSA, middle), and asymmetry parameter (g, right) for each of our optical lookup tables considered in this study. Results presented are for the climatological particle size distribution at Cape Verde from our OPAC-Spheres simulation normalized to an AOT of 1 at 550 nm. Absolute values (top) and differences from the OPAC-Spheres values (bottom) are presented.

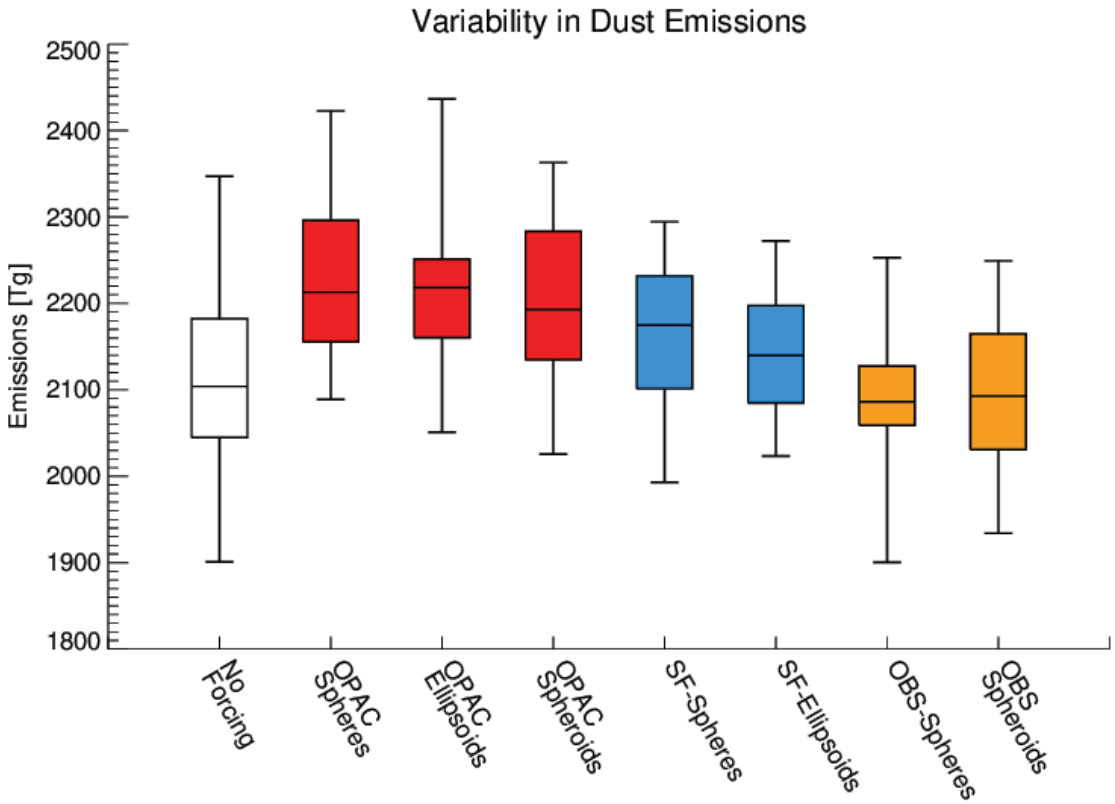

1158
1159 **Figure 3.** 2011 – 2050 climatology of annual mean dust emissions [Tg yr^{-1}] for each of our
1160 simulations. We show the mean (horizontal line), inner quartile range (box), and extrema
1161 (whiskers) of the time series.

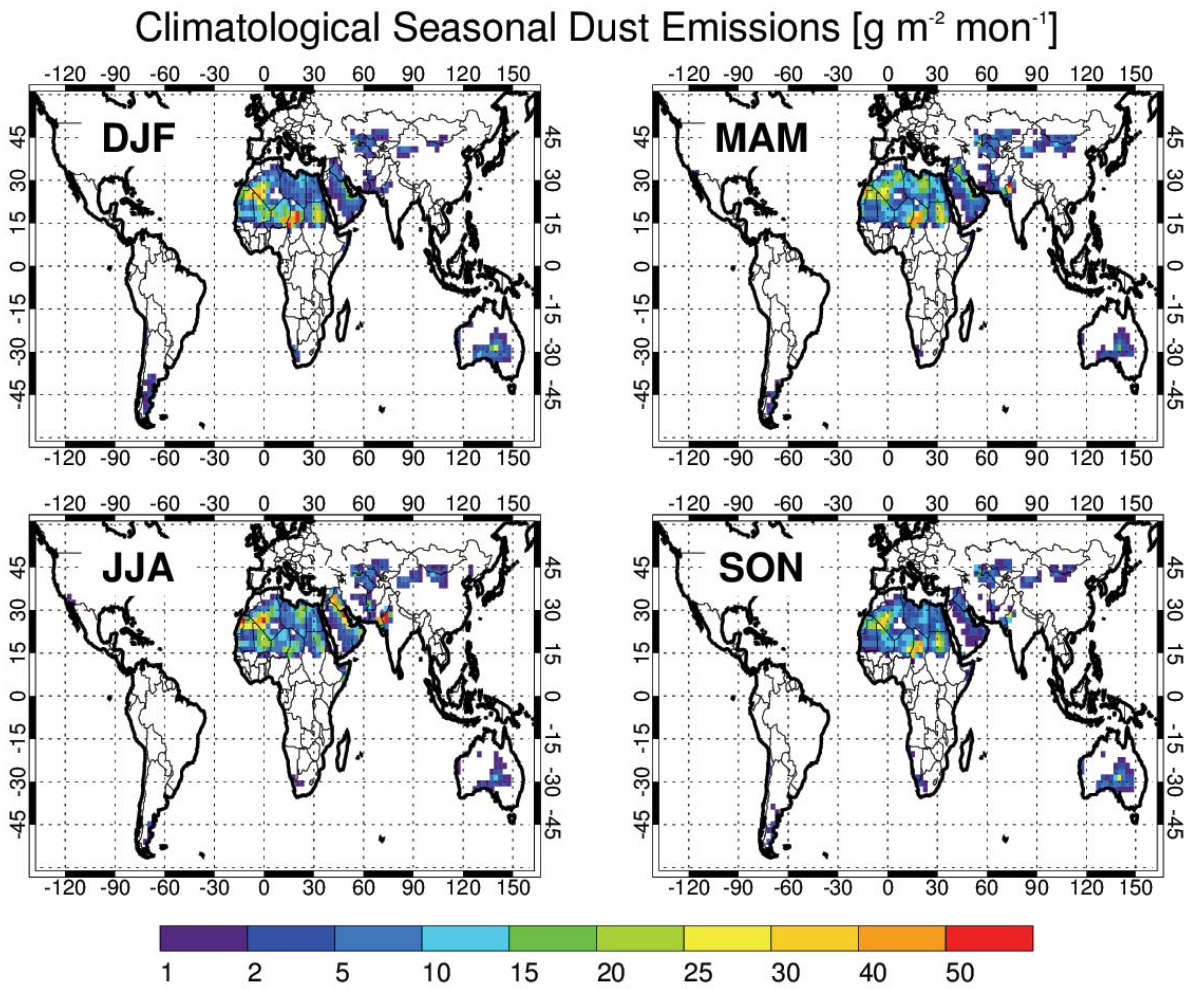

Figure 4. Years 2011 – 2050 climatology of seasonal dust emissions for our No Forcing simulation.

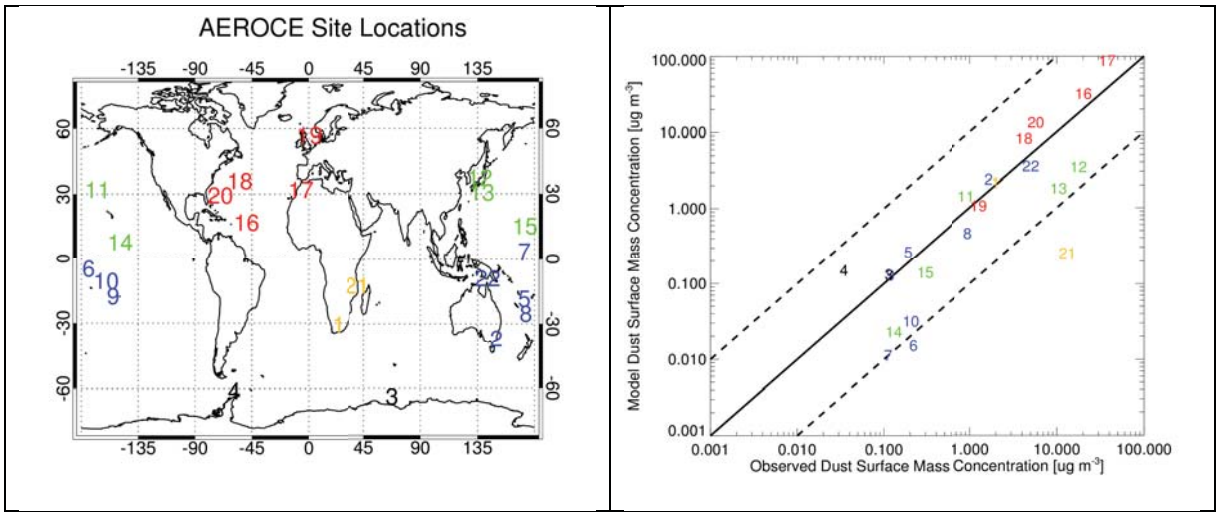

Figure 5. Map of dust surface mass concentration sites summarized in Table 3. Also shown is a scatter plot of the OPAC-Spheres modeled climatological mean surface mass concentration compared to the multi-year observations at each site. The one-to-one line is indicated by a solid line. The dashed lines show the ten-to-one and one-to-ten lines. Colors correspond to broad geographical regions to facilitate analysis of scatter plot.

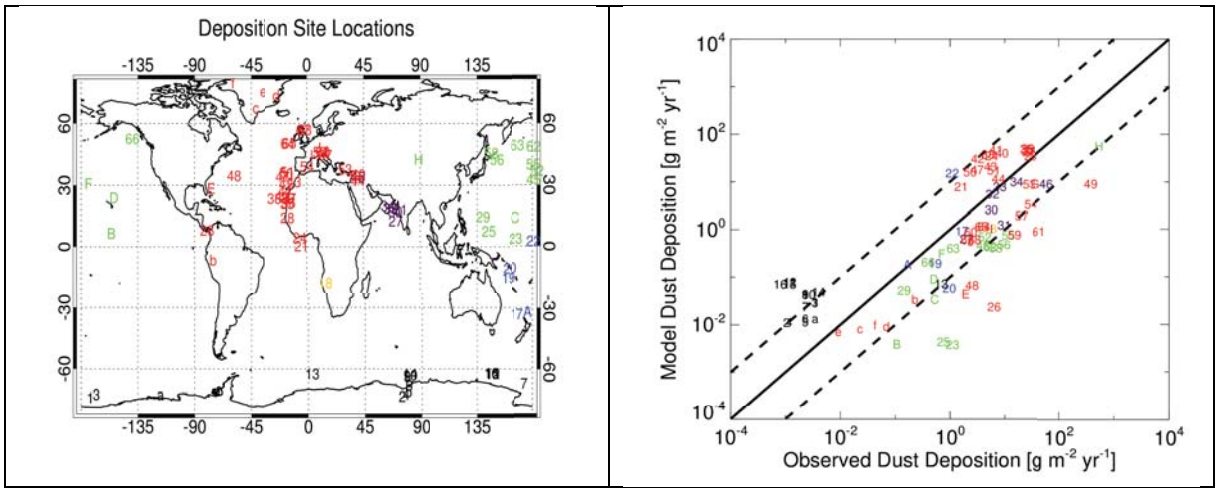

Figure 6. As in Figure 5, but dust deposition sites listed in Table S2.

1171

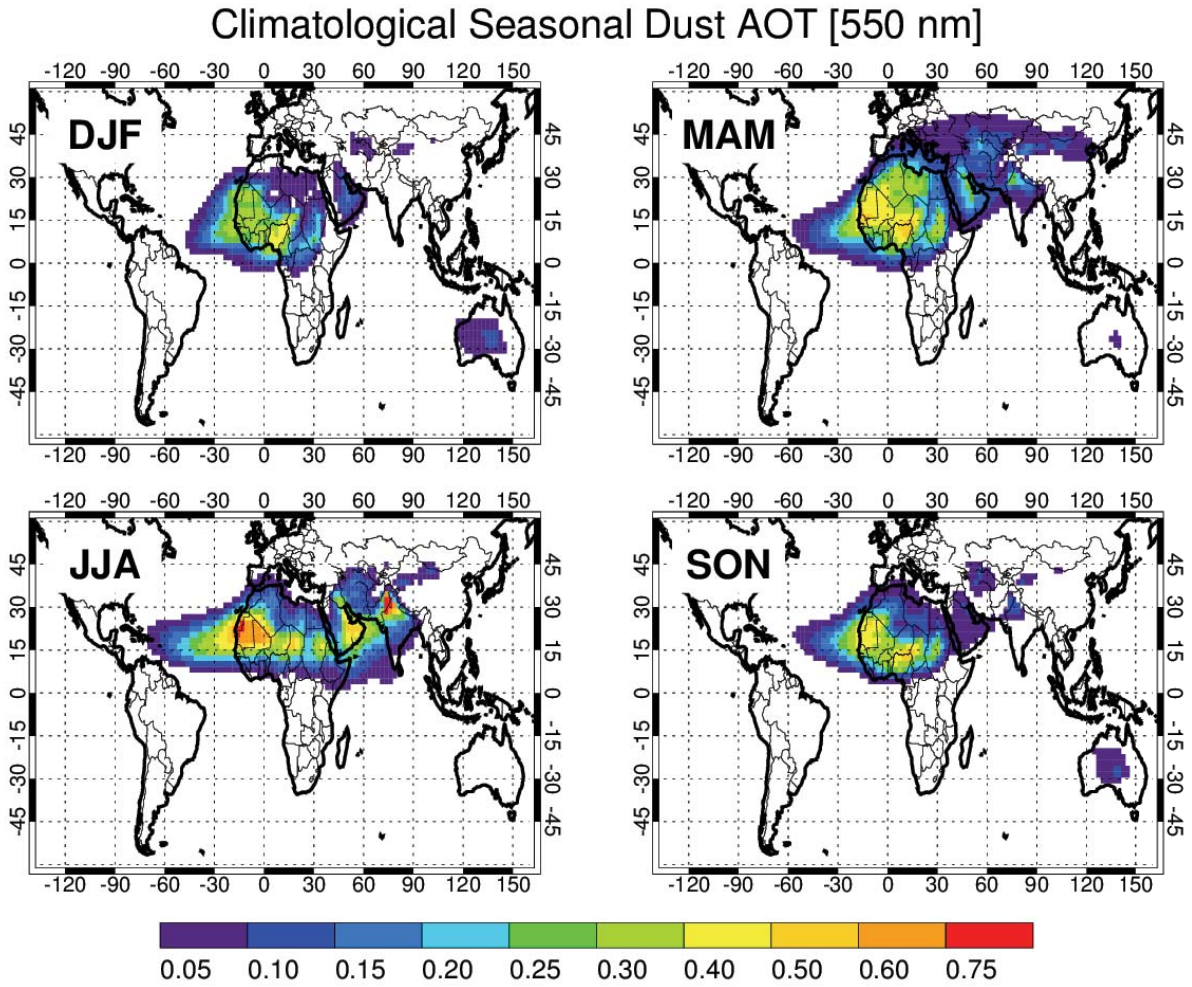

1172

1173 **Figure 7.** Years 2011 – 2050 climatology of seasonal 550 nm dust AOT for our No Forcing
1174 simulation.

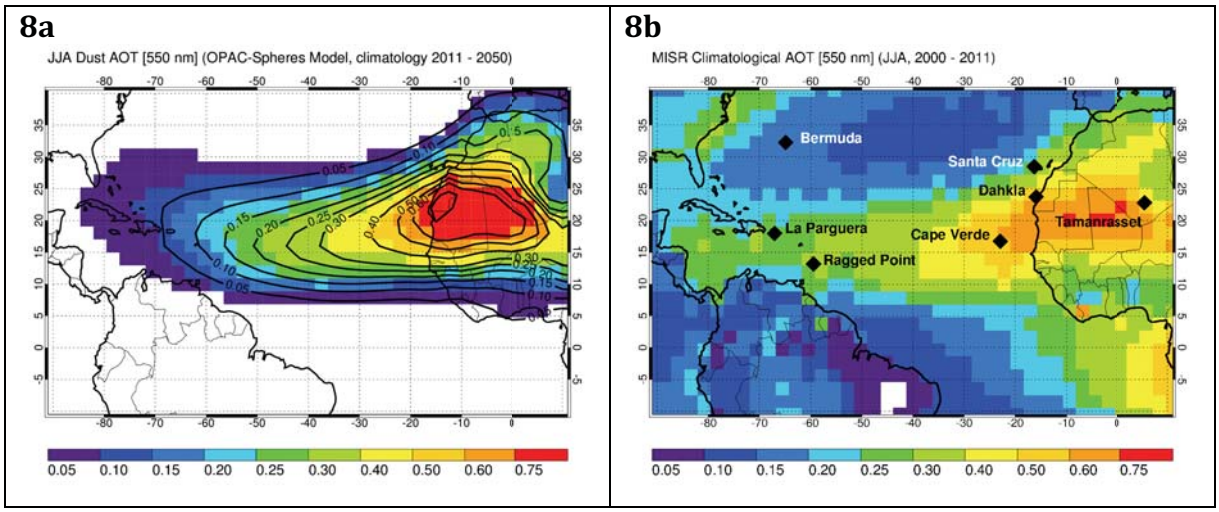

Figure 8. Climatological JJA aerosol optical thickness from the OPAC-Spheres (shading) and No Forcing (contours) model runs (left, dust only) and MISR observations (right). Also shown are the locations of the AERONET sites used in this study.

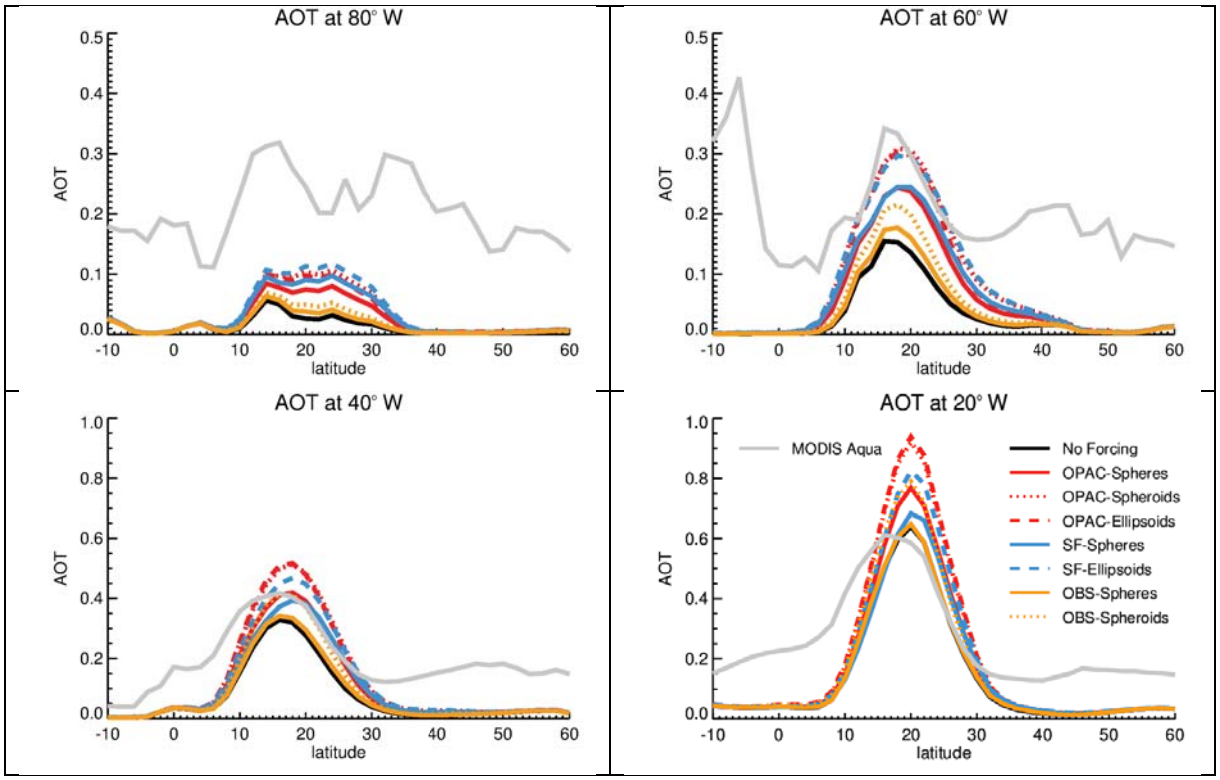

Figure 9. Climatological simulated JJA dust AOT at four different longitudes west of northern Africa. Also shown is the MODIS Aqua over ocean AOT climatology for JJA 2002 – 2011.

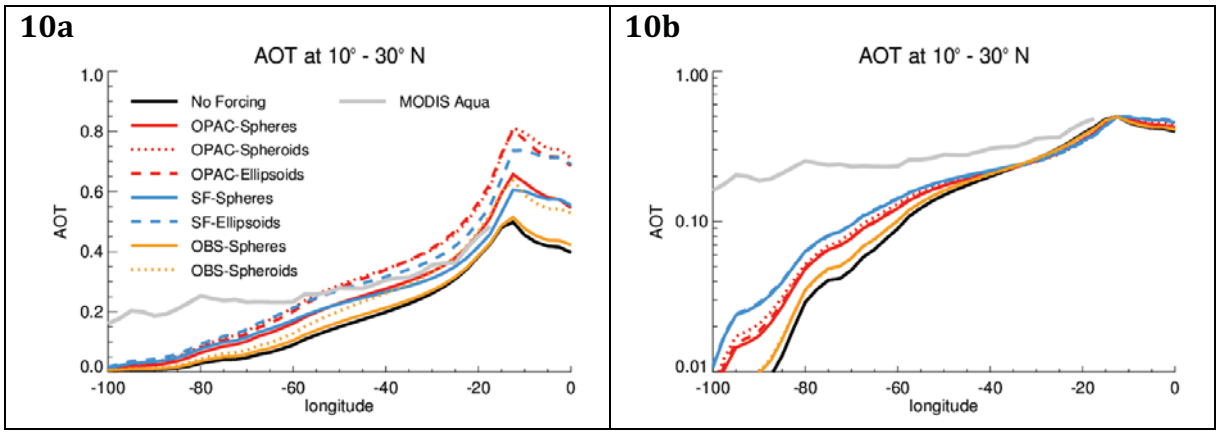

Figure 10. Climatological JJA dust AOT in the latitude band 10° - 30° N for our simulations for the years 2011 – 2050. Also shown is the climatological JJA MODIS Aqua over ocean AOT averaged over the period 2002 – 2011. At left the results are plotted on a linear scale. At right the model and satellite values are normalized to the same value of AOT at the longitude of Cape Verde and the results are plotted on a log-y axis to emphasize differences in the simulations.

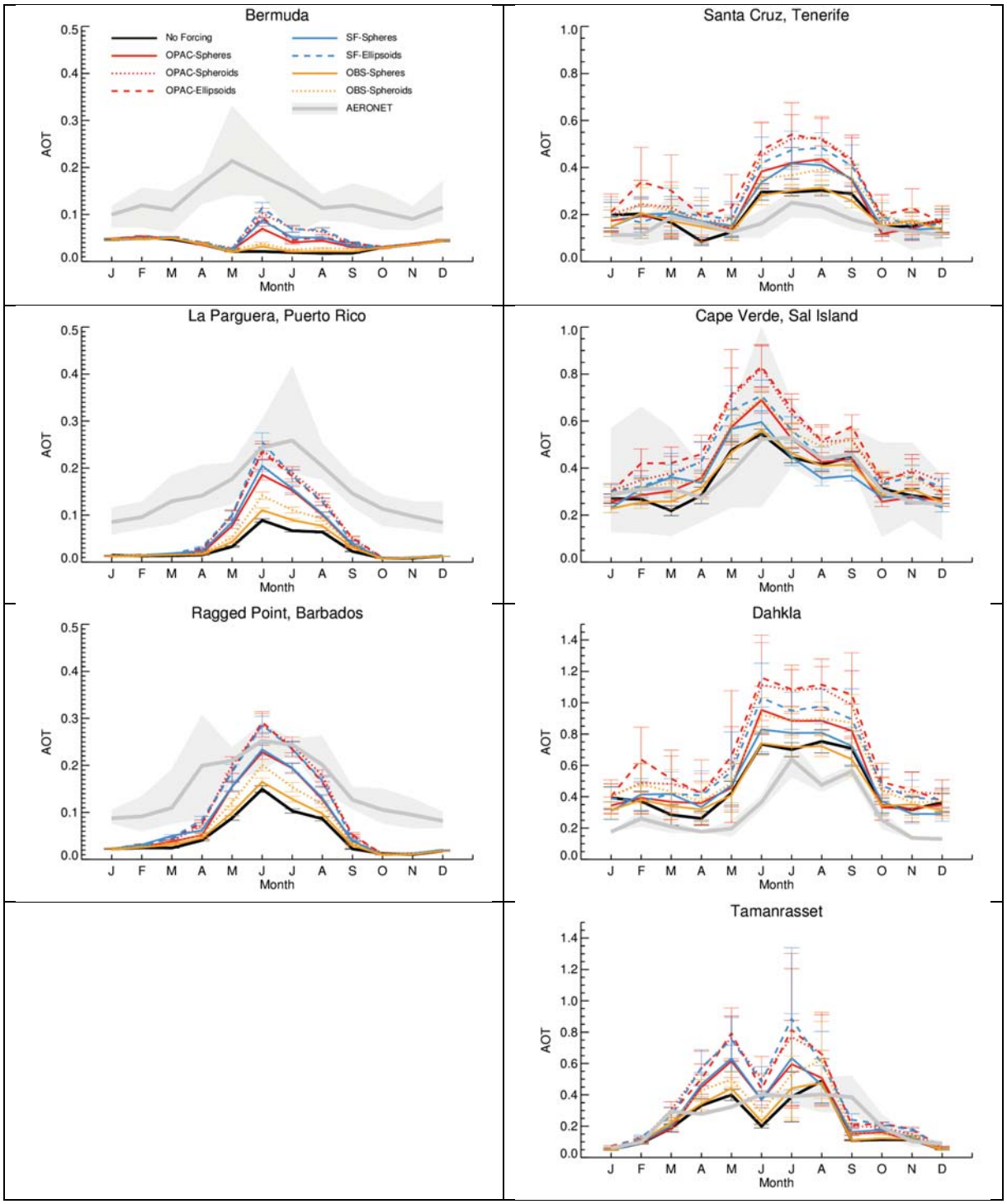

1187 **Figure 11.** Comparison of climatological monthly mean AOT from our simulations to
1188 multi-year monthly means from AERONET at seven sites impacted by Saharan dust. The
1189 whisker bars indicate the standard deviation of the monthly mean values. The sites are
1190 described in Table 4 and their locations shown in Figure 8. The AERONET mean and
1191 standard deviations are indicated by the grey line and light grey shading.

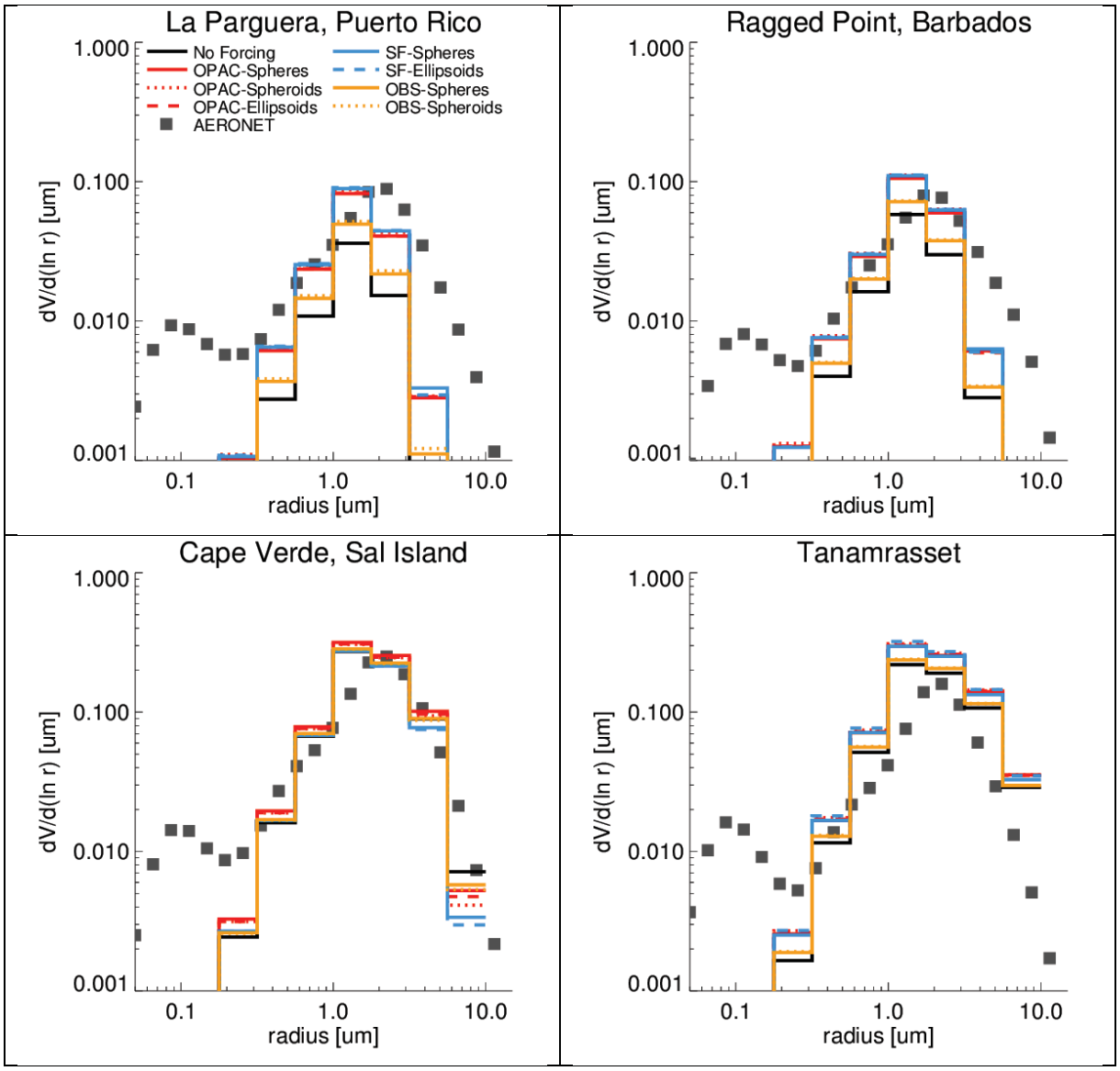

1192 **Figure 12.** Comparison of JJA climatological simulated dust particle size distribution
1193 (lines) to the seasonal multi-year AERONET retrieved particle size distribution at four
1194 AERONET sites.

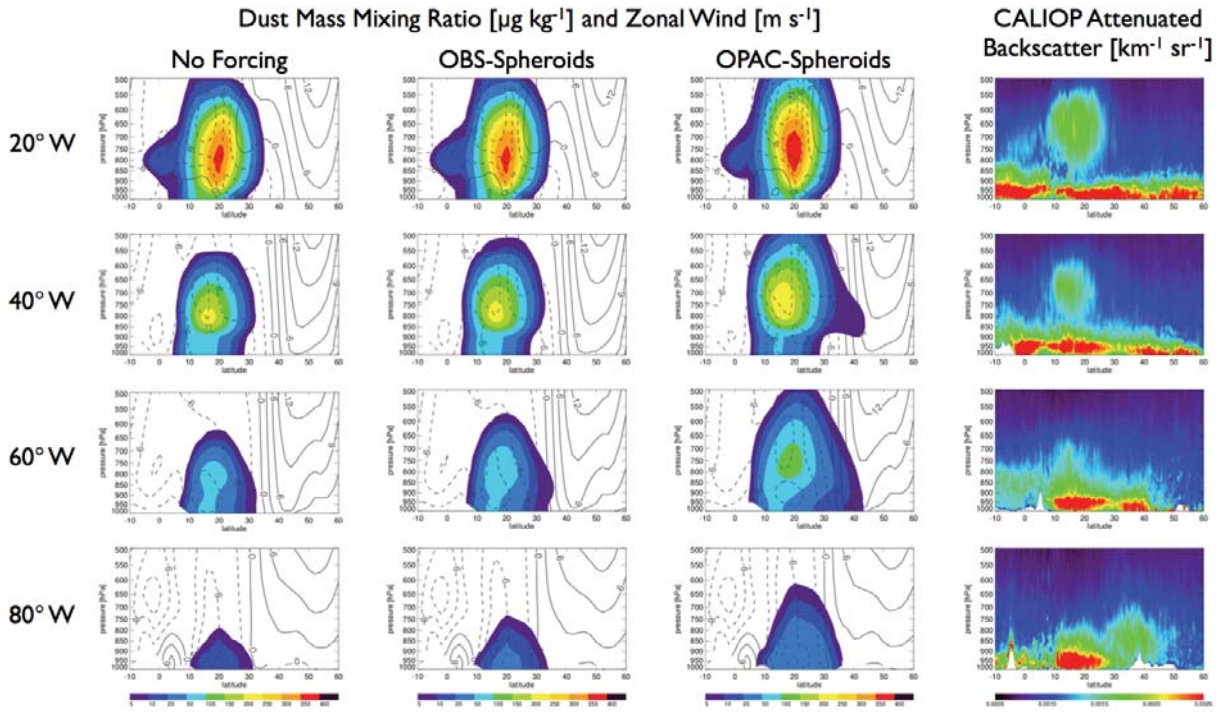

Figure 13. Simulated JJA climatological dust mass mixing ratio profiles at four longitudes west of the Saharan source region. Results are shown for three model simulations, as well as the year 2011 seasonal attenuated backscatter measured by CALIOP (right column). On the model plots we also show the profile of the climatological seasonal mean zonal wind. White regions at the surface in the CALIOP plots are below the local topography.

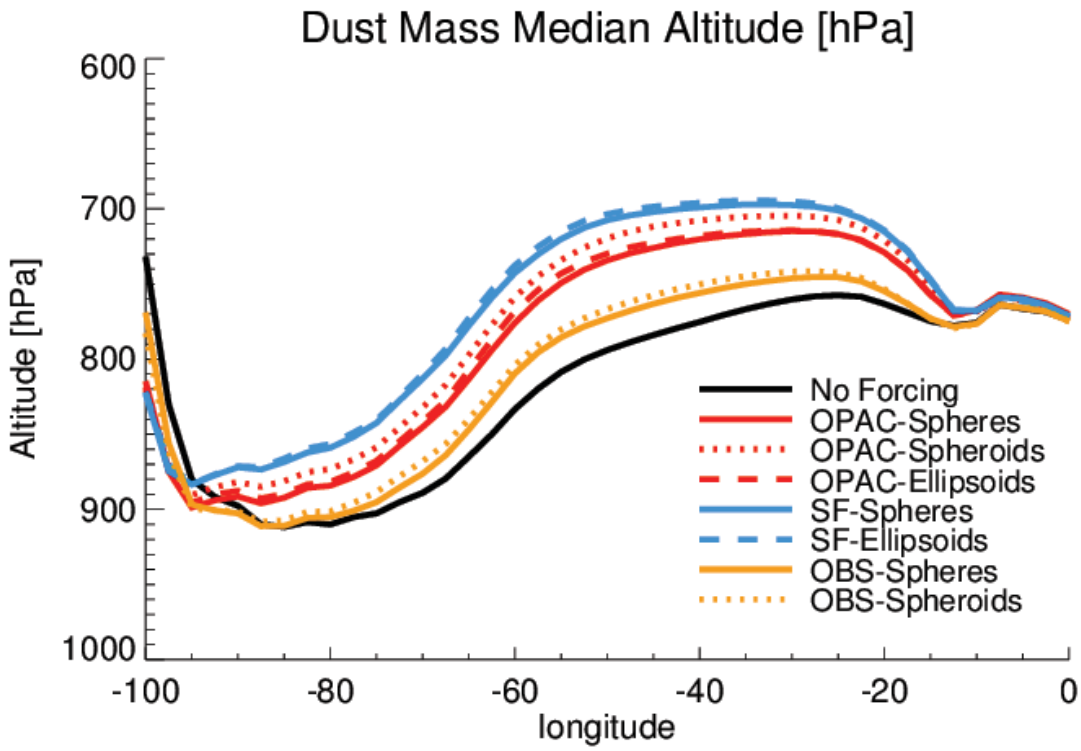

1201
1202 **Figure 14.** Dust median altitude for each of simulations. Results are shown for the JJA
1203 climatological mean value averaged in the latitude range 10° - 30° N.

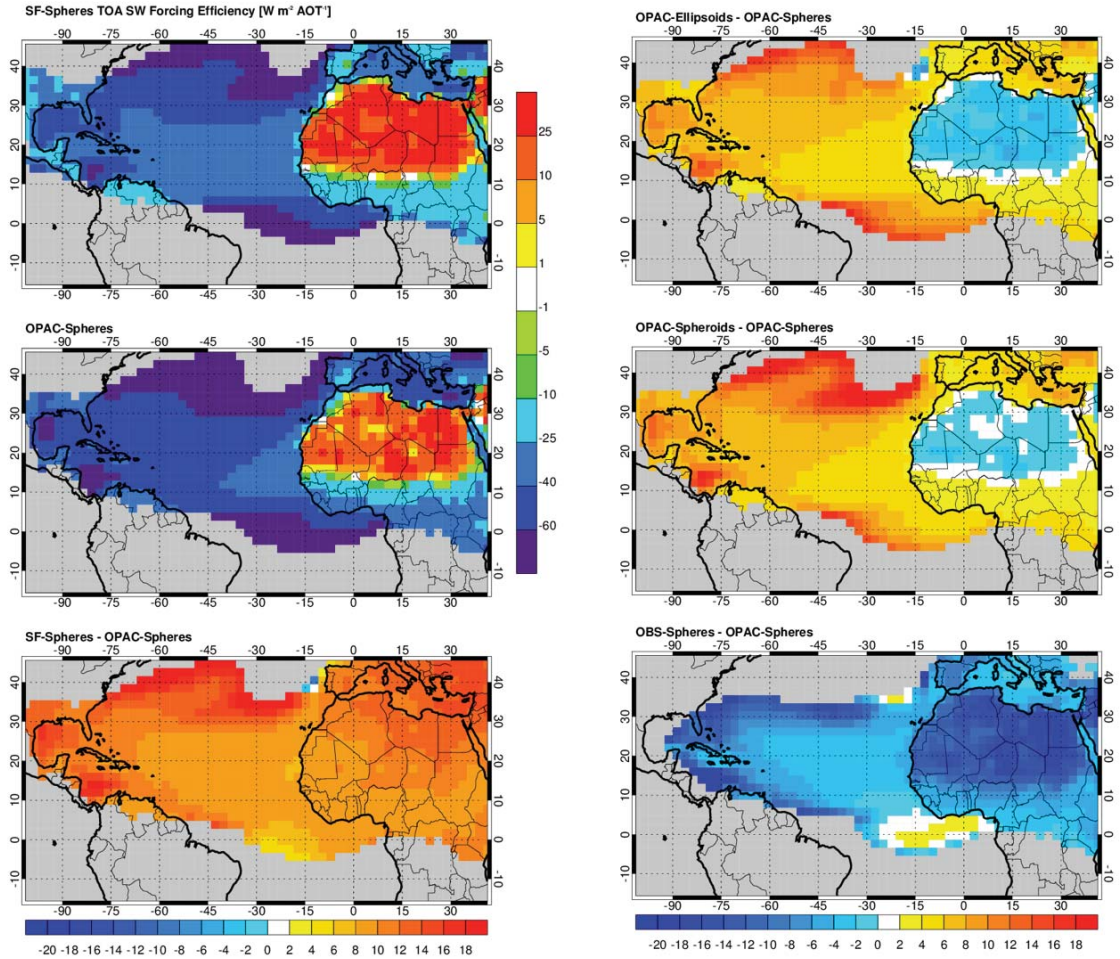

Figure 15. JJA climatology of TOA shortwave aerosol forcing efficiency. At left we show the SF-Spheres and OPAC-Spheres values, as well as their difference. At right we show the difference only for the OPAC-Ellipsoids, OPAC-Spheroids, and OBS-Spheres simulations relative to the OPAC-Spheres baseline.

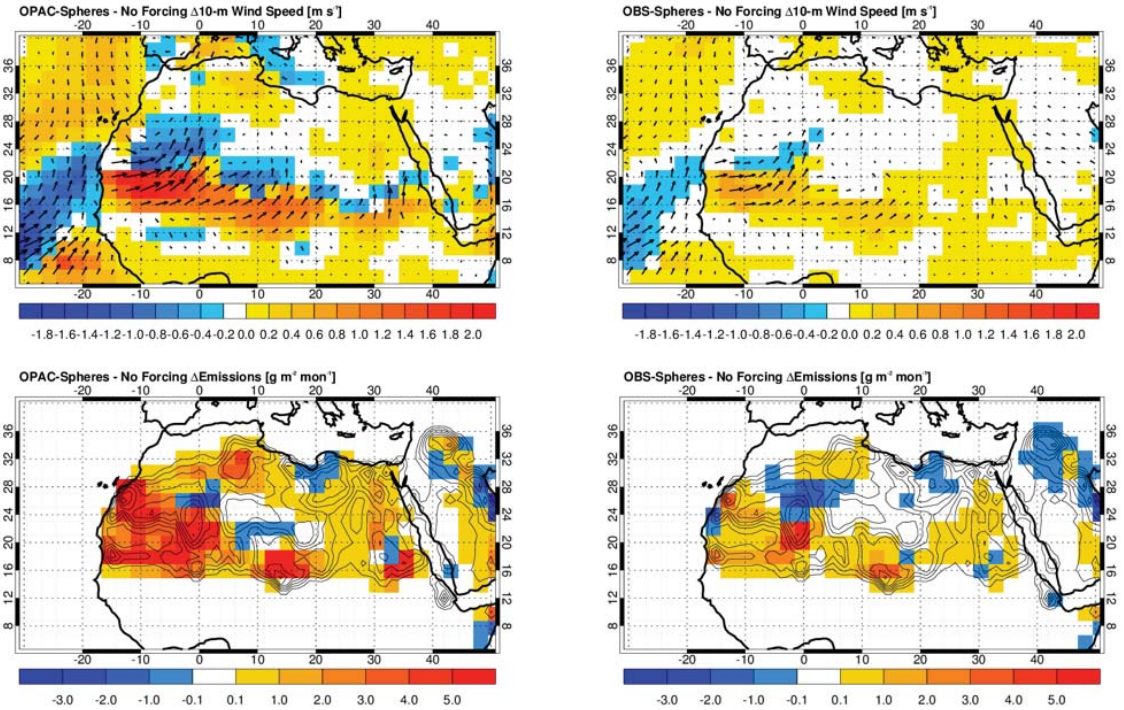

Figure 16. JJA climatology of difference in mean surface wind speeds (top) and dust emissions (bottom) relative to the reference No Forcing simulation. Differences are shown for the OPAC-Spheres (left) and OBS-Spheres (right) simulations.

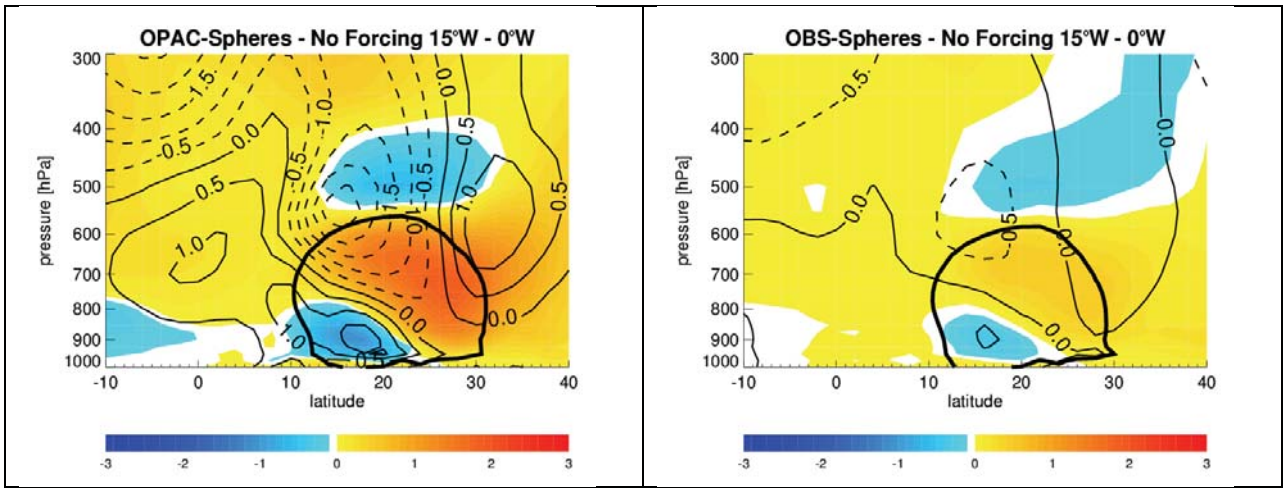

Figure 17. JJA climatology of difference in mean zonal temperature profile (shading) and zonal wind speed (thin contours) averaged 15° W - 0° against the reference No Forcing simulation. The differences are for the OPAC-Spheres simulation (left) and the OBS-Spheres simulation (right). The thick contour shows the 100 μg m^{-3} dust concentration isosurface for the perturbation experiments to indicate maximum dust concentrations.

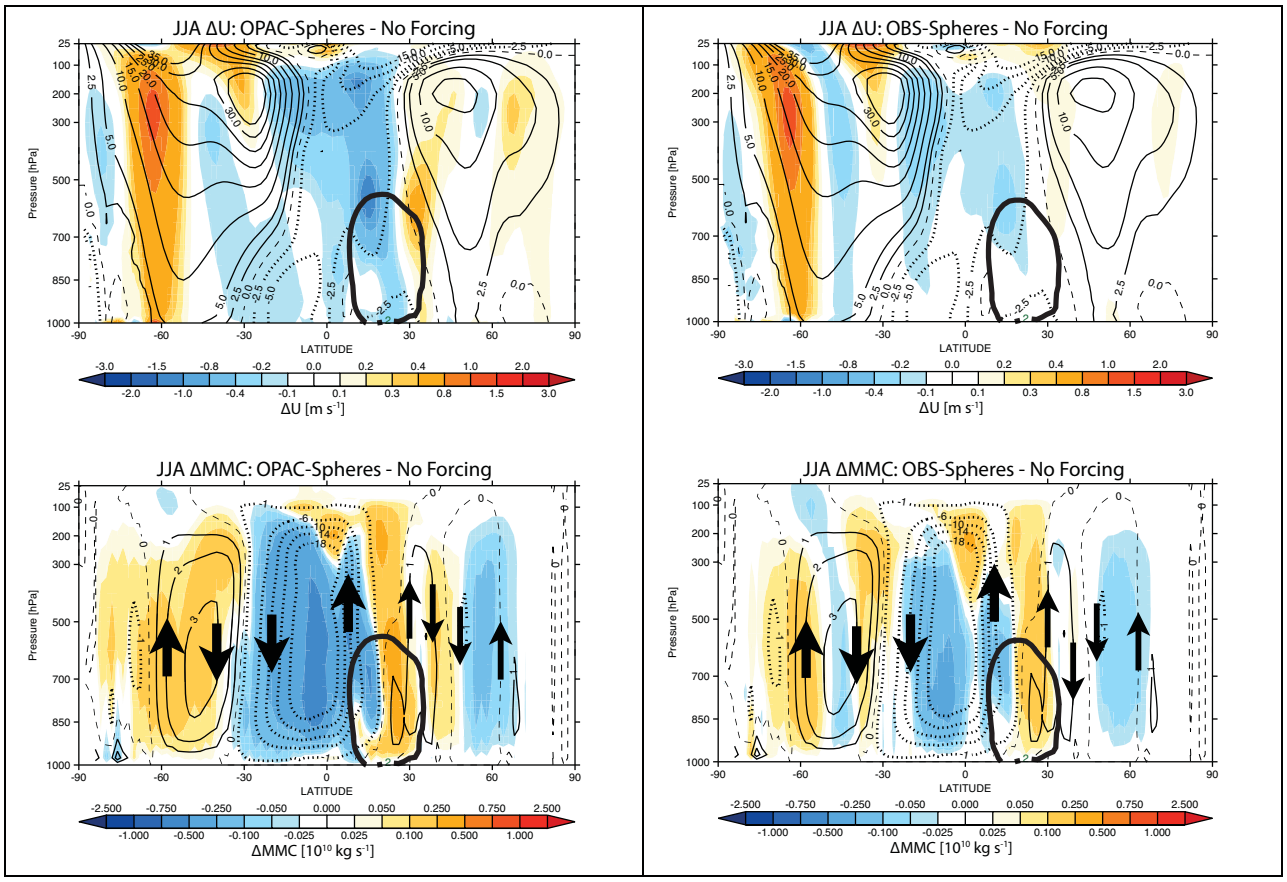

Figure 18. JJA climatology of zonal averaged zonal wind (top) and mean meridional circulation (bottom). Contour lines show the values of the reference No Forcing simulation, while the shading shows the difference of the OPAC-Spheres (left) and OBS-Spheres (right) relative to the reference simulation. The thick contour shows the 20 μg m^{-3} dust concentration isosurface to indicate maximum dust. The arrows give a qualitative sense of the vertical transport. For the mean meridional circulation, negative values indicate counterclockwise transport (contours) or an increase in the counterclockwise transport (shading).